AGU PUBLICATIONS

JGR

Journal of Geophysical Research: Planets

RESEARCH ARTICLE

10.1002/2015JE004824

Key Points:

- Eddy activity is zonally modulated and significantly interannually repeatable
- Eddy propagation follows topographic features such as Tharsis
- The topography-following behavior is stronger at the surface than at higher altitude

Supporting Information:

- Tables S1 and S2

Correspondence to:
T. A. Mooring,
tmooring@alum.mit.edu

Citation:
Mooring, T. A., and R. J. Wilson (2015), Transient eddies in the MACDA Mars reanalysis, *J. Geophys. Res. Planets*, *120*, 1671–1696, doi:10.1002/2015JE004824.

Received 24 MAR 2015
Accepted 14 SEP 2015
Accepted article online 19 SEP 2015
Published online 24 OCT 2015

Transient eddies in the MACDA Mars reanalysis

Todd A. Mooring[1] and R. John Wilson[2]

[1] Program in Atmospheric and Oceanic Sciences, Princeton University, Princeton, New Jersey, USA, [2] Geophysical Fluid Dynamics Laboratory, NOAA, Princeton, New Jersey, USA

Abstract We present a survey of the transient eddy activity in the Mars Analysis Correction Data Assimilation (MACDA) reanalysis. The spatial structure and propagation characteristics of the eddies are emphasized. Band-pass-filtered variance and covariance fields are found to be zonally modulated, indicating a longitude dependence of the typical amplitudes of Martian transient eddies. Considerable repeatability of the eddy field spatial structures is found across Mars years, including a roughly wave number 3 pattern of low-level eddy meridional temperature transport ($\overline{v'T'}$) in the northern hemisphere that is evident before and after winter solstice and a possible tendency for northern hemisphere eddy kinetic energy maxima to be located above low-lying areas. Southern hemisphere eddy fields tend to feature two local maxima, one roughly south of Tharsis and the other associated with Hellas. Eddies are weakened near winter solstice in both hemispheres and were generally weakened in the northern hemisphere during the 2001 (Mars year 25) global dust storm, albeit with little change in spatial patterns. Because the transient eddies propagate in space, we also used a teleconnection map-based technique to estimate their phase velocities. Eddy propagation at the surface is found to follow topography, a phenomenon less evident at higher altitude. Possible physical mechanisms underlying the documented eddy phenomena are discussed.

1. Introduction

Transient eddies in the Martian atmosphere have been a subject of quantitative study for more than half a century. Prior to the first successful Mars missions *Mintz* [1961] sought to use the two-level model to study the existence, scale, and seasonality of baroclinic eddies on the planet. Transient eddies also appeared in the initial Mars general circulation model (GCM) simulations of *Leovy and Mintz* [1969]. Early major empirical studies include *Barnes* [1980, 1981], which analyzed surface weather observations from the Viking landers to tentatively identify the synoptic-scale variability as baroclinic eddies and estimate their horizontal wave numbers and phase speeds.

The extent to which Martian transient eddies can be characterized from measurements at two surface stations is inherently limited, and the observational study of the eddies has been greatly advanced by the availability of data from the Mars Global Surveyor Thermal Emission Spectrometer (TES). The most extensive survey to date of the transient eddies is *Banfield et al.* [2004], which identified traveling waves in the TES temperature fields and documented the seasonal evolution of their amplitude, phase structures, zonal modulation, and other properties.

Much of the existing literature on Martian transient eddies emphasizes their zonal coherence and describes them in terms of zonal wave number. Although attempts to characterize nonzonal eddy propagation are not new [*Barnes*, 1981], this phenomenon has apparently received little previous attention. The zonal wave number view is also limited in its ability to describe zonal modulation of transient eddy amplitude, despite the prediction of such modulation by Mars general circulation models [*Hollingsworth et al.*, 1996, 1997] and observational evidence of its existence [*Banfield et al.*, 2004; *Hinson et al.*, 2012]. Furthermore, the zonal modulation of eddy activity (and possibly also nonzonal eddy propagation behavior) is relevant to initiation of flushing dust storms, which transport dust southward through the northern hemisphere lowlands and form an important component of the Martian dust cycle [e.g., *Wang et al.*, 2003, 2005; *Wilson et al.*, 2006; *Cantor*, 2007; *Hinson and Wang*, 2010; *Wang and Richardson*, 2015].

Banfield et al. [2004] identified the transient eddy component of the Martian atmospheric temperature field by binning the data in space and time and subtracting 50 Martian solar day (sol) running means. For studies of the waves' meridional transports, they used balance relationships to estimate transient eddy horizontal winds but found that usable results could be obtained only for wave number 1.

An alternative approach to casting the lengthy series of TES measurements into a form more amenable to analysis is data assimilation, using a GCM to spread the information contained in temperature profiles and column dust opacities in time, space, and to other atmospheric variables not directly observed [*Lewis et al.*, 2007a]. Virtually any atmospheric phenomenon occurring on spatial scales resolved by the GCM may then be studied in the resulting estimate of the evolving atmospheric state.

In this paper, we present an extensive characterization of Martian transient eddies as represented in the Mars Analysis Correction Data Assimilation (MACDA), a publicly available data set created by using the UK Mars GCM to assimilate TES temperature and dust opacity retrievals [*Montabone et al.*, 2006; *Lewis et al.*, 2007a; *Montabone et al.*, 2014]. We build on the studies of *Lewis et al.* [2007b] and *Lewis et al.* [2008], who obtained some of our results in much shorter papers by analyzing a predecessor of MACDA. Although we discuss the characteristic zonal wave numbers of Martian eddies as have previous works, we emphasize the horizontal structure of eddy variance-covariance fields and other spatially local diagnostics of eddy properties [e.g., *Wallace et al.*, 1988; *Chang et al.*, 2002]. Such data analysis techniques have been used in terrestrial atmospheric studies for years but benefit from or require a multivariate gridded data set not previously available for Mars. Our results provide an improved view of the horizontal distribution of transient eddy activity and a new perspective on the eddies' propagation characteristics.

Multivariate gridded output from Mars GCMs has been available for decades, but we believe MACDA is likely an improvement on the free-running version of its underlying GCM (and perhaps an improvement on all free-running Mars GCMs) because data assimilation has apparently increased the realism of the low-level transient eddies. Our comparisons of MACDA to a free-running control simulation with the same GCM (forced with the same observationally-based dust distribution) show that MACDA exhibits a solstitial pause [*Read et al.*, 2011; *Lewis et al.*, 2015] in northern hemisphere eddy activity near L_s 270° in each of the three available Mars years, which is absent in the free-running simulation [cf. *Mulholland et al.*, 2015]. Since this solstitial pause is visible in TES observations directly [*Banfield et al.*, 2004; *Wang et al.*, 2005] and is independently evidenced by dust storm and cloud imagery [*Read et al.*, 2011; *Lewis et al.*, 2015], it is most likely a feature of the real world represented in MACDA only because of the temperature data assimilation.

Other works have systematically documented deficiencies in the simulation of low-altitude eddies by free-running Mars GCMs [*Kavulich et al.*, 2013; *Wang et al.*, 2013]. The latter study indicates that subtle changes in the zonal mean structure of the polar vortex can have a significant impact on simulated eddy activity. Indeed, comparisons of the zonal mean temperatures in MACDA (which are in excellent agreement with raw TES data) with those in the control simulation reveal significant biases in polar temperatures that are apparently largely due to the specification of the vertical distribution of dust in the model [*Wilson et al.*, 2008]. Recent work has indicated that inclusion of radiatively active water ice clouds in simulations can have a significant impact on traveling wave activity [*Wilson*, 2011; *Kahre et al.*, 2012; *Barnes et al.*, 2014]. The data assimilated into MACDA implicitly represent the impact of aerosols on temperature structure, providing a theoretical basis for expecting MACDA to have more realistic eddies than a free-running Mars GCM.

Section 2 of the paper describes the MACDA data set in more detail, explains how the transient eddies were extracted from it for analysis, and presents an example of the use of MACDA data to study a dust storm. Section 3 discusses the zonal scales of the eddies, while the spatial structures of several major eddy variance-covariance fields and their seasonal and global dust storm-related changes are described in section 4. Eddy phase velocity fields are presented in section 5, and section 6 discusses the physical interpretation of the results and identifies caveats associated with the MACDA data set. A seventh section synthesizes the results and concludes.

2. Data Set, Eddy Extraction, and Flushing Dust Storm Case Study

The observational basis of the MACDA data set is nadir retrievals of temperature and column dust opacity collected by TES from Mars Global Surveyor's Sun-synchronous mapping orbit. In its native form, the data set is available on 25 sigma levels at 5° horizontal resolution. (The sigma vertical coordinate is defined as $\sigma = p/p_s$, where p is the pressure at the point of interest in three-dimensional space and p_s is the surface pressure at the same horizontal position [*Phillips*, 1957].) To extract the transient eddy component of the fields of interest,

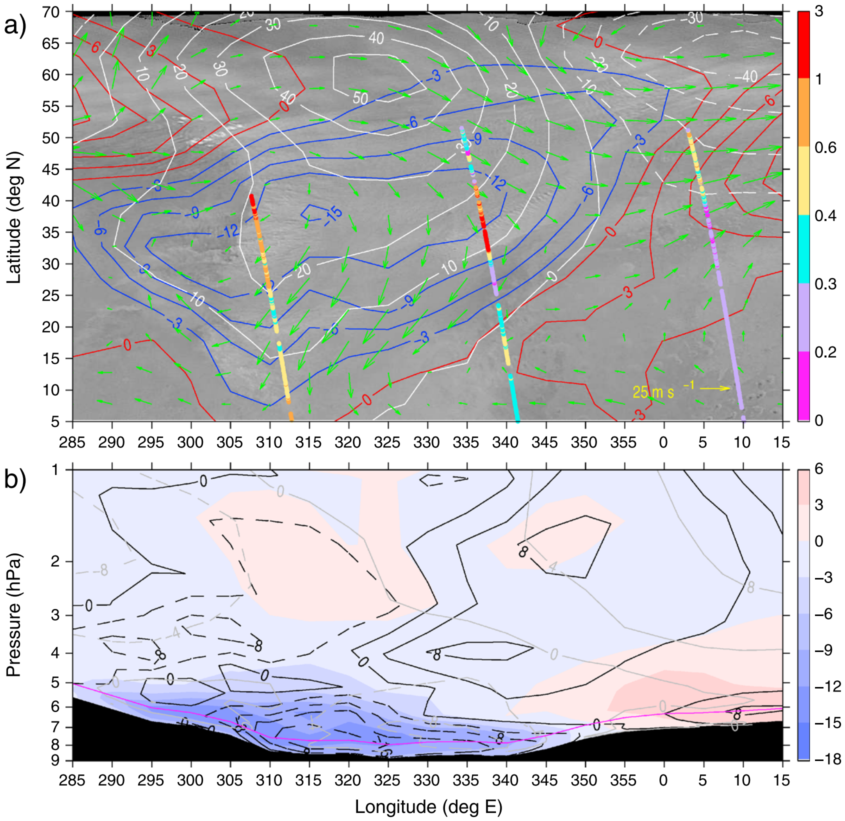

Figure 1. MACDA fields combined with a Mars Orbiter Camera image and TES column dust opacity retrievals to analyze a flushing dust storm in Acidalia/Chryse. The MOC image was grayscaled by stripping the red component from a color image, while the dust optical depths (thick multicolored lines) have been normalized to units of optical depth per 6.1 hPa. Instantaneous MACDA fields are shown at MY24 L_s 223.79° (labeled 223.92° in the MACDA data set itself, see discussion in main text), approximately the same as the time at which the dust opacity data near 340°E was recorded. (a) All of the MACDA data are instantaneous, with eddy surface pressure (Pa) contoured in white. Eddy temperature (K) is contoured in red and blue and full wind fields are shown with green arrows, both on $\sigma = 0.8996$. The wind vectors are drawn parallel to the streamlines of the wind field and have lengths proportional to the wind speed (a scale arrow is shown in yellow). (b) Vertical section at 32.5°N. The eddy temperatures (K, red and blue shading) and meridional winds (black contours, m s^{-1}) are instantaneous. The quasi-stationary component of the meridional wind field is plotted as well (gray contours, m s^{-1}) and was derived by averaging the winds on their native sigma surfaces over a 30 sol window nearly centered on L_s 223.79°, then converting to pressure coordinates using mean surface pressures over the same time interval. To aid comparisons between the two panels, the $\sigma = 0.8996$ surface has been marked in Figure 1b with a magenta line.

we use a band-pass filter to remove the thermal tide, quasi-stationary waves, and the seasonal cycle. The half power points of the band-pass filter are located at 1.24 and 15.36 sols. Low-level transient eddies in MACDA are found to have periods of 2 to 8 sols, which are well within this passband. Traveling waves with longer periods of 10 to 30 sols are sometimes observed at higher altitudes but are not considered in the current study as they may be dynamically distinct from the lower level waves—the upper level waves have been suggested to be partly manifestations of inertial, as well as baroclinic and barotropic, instability [e.g., *Barnes et al.*, 1993; *Wilson et al.*, 2002; *Banfield et al.*, 2004].

An example of MACDA flow fields and their potential for illuminating atmospheric dynamics and dust storm behavior is shown in Figure 1. Figure 1a shows instantaneous eddy surface pressures, eddy temperatures, and full wind fields at $\sigma = 0.8996$ (roughly 1 km above ground level), superimposed on a contemporaneous image from the Mars Global Surveyor Mars Orbiter Camera (MOC) [*Cantor et al.*, 2001] and TES column dust opacity retrievals [*Smith*, 2004]. Figure 1b shows a vertical section at 32.5°N that depicts eddy temperatures and meridional winds as well as 30 sol mean meridional winds. The horizontal distribution of eddy temperature is qualitatively consistent with geostrophic advection along the pole-equator temperature gradient, and the full wind field is consistent with southward transport of the dust. Comparison of Figures 1a and 1b suggests a

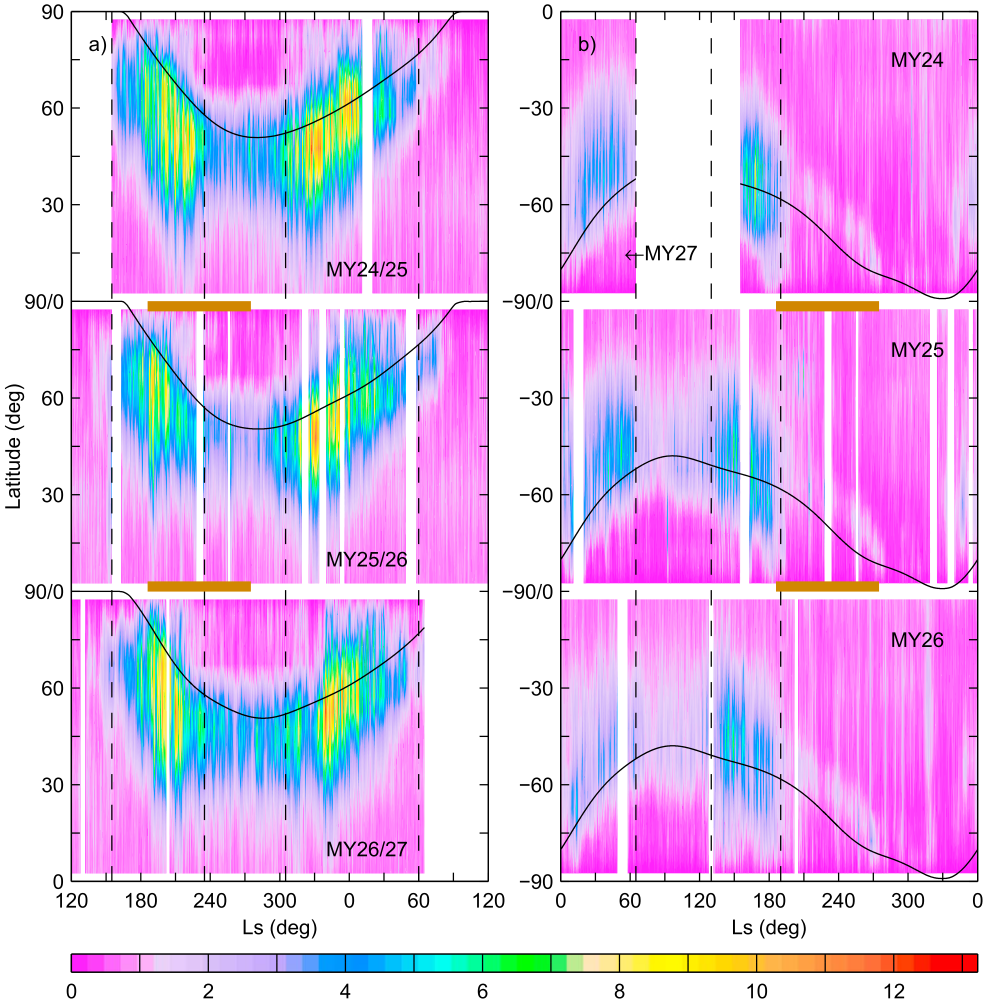

Figure 2. The seasonal and meridional distribution of lower-atmospheric eddy activity in MACDA is depicted in this plot of the zonal standard deviation of eddy temperature (K) at $\sigma = 0.8996$ (~1 km above ground level). (a) Northern hemisphere and (b) southern hemisphere eddy activity. For both hemispheres, data are plotted for MY24 L_s 155° to MY27 L_s 65°, with time generally increasing from left to right and down the rows of each panel. Vertical black dashed lines delineate the four seasons defined in Table 1. The temporal extent of the MY25 global dust storm (here taken as L_s 186°–275°) is indicated by the horizontal brown bars above and below the relevant section of MY25 data. Zonal standard deviation eddy temperatures are not plotted during 10 significant temporal gaps in the availability of TES data to assimilate (Table S1). The solid black lines indicate zonal mean CO_2 cap edges derived from TES data [*Titus and Cushing*, 2014]. Northern hemisphere cap edge data are available over the full length of MACDA, but the plotted southern cap edge is a nominal value based on data for MY25 L_s 297° to MY26 L_s 297°. Note that this cap edge data set is distinct from the surface CO_2 ice data produced by and available as part of MACDA.

substantial contribution by the eddy winds to the full wind field and indicates that this eddy is strongest very near the surface. Such results motivate our particular interest in low-level transient eddies.

Figure 2 displays the zonal standard deviation of eddy temperature at $\sigma = 0.8996$ as a function of latitude and time. This sigma surface was chosen for use here and in section 3 because low-level eddies have relatively large amplitudes on it—for example, it is the level of the northern hemisphere meridional and lower atmosphere ($\sigma > 0.4553$) vertical maximum in annual mean zonal mean eddy temperature standard deviation. Both hemispheres are seen to exhibit an essentially repeatable seasonal cycle, with eddy activity strongest before and after winter solstice but weakened near the solstice itself to form a solstitial pause [*Read et al.*, 2011; *Lewis et al.*, 2015]. Comparably designed figures for eddy temperature at 2.5 km above ground level and meridional wind at 4 hPa are shown as Figure 1 of *Lewis et al.* [2015] and Figure 6 of *Lewis et al.* [2007b], respectively, and for eddy temperature at 5.7 hPa as Figure 7 of *Kavulich et al.* [2013]. Unsurprisingly, they all have similar content. This seasonal pattern is similar to that found in the TES retrievals themselves for the northern hemisphere at

Table 1. Season Definitions For Analysis of MACDA Transient Eddy Activity

Season Name	NH L_s Range (°)	SH L_s Range (°)
PRE	155–235	0–65
PAUSE	235–305	65–130
POST	305–60	130–190
SUMMER	60–155	190–0
DUST	186–275	186–275

4.75 hPa by *Wang et al.* [2005], as illustrated in their Figure 8. The eddies are also clearly substantially stronger in the northern hemisphere than in the southern hemisphere, as predicted by *Barnes et al.* [1993] and confirmed by *Banfield et al.* [2004]. To best capture the seasonal cycle of eddy activity in subsequent analyses, we examined plots similar to Figure 2 and chose a set of season definitions that would accentuate the pattern qualitatively described above. Names for the seasons and precise definitions as L_s ranges are given in Table 1, and their edges are marked in Figure 2. A fifth season (DUST) covers the L_s range of the Mars year (MY) 25 global dust storm.

Although the MACDA data set extends continuously from MY24 L_s 141° to MY27 L_s 86°, the TES instrument was not always collecting data, leading to brief periods in which MACDA was relatively unconstrained by the observations. Breaks in the availability of data to assimilate can result in rapid, physically unreasonable changes in the MACDA state [*Montabone et al.*, 2014], including major distortions of eddy activity clearly visible in plots similar to Figure 2. Accordingly, we used information on the number of temperature retrievals assimilated in 2° latitude × 1° L_s bins to identify 14 significant data gaps during which both day and night retrievals were largely or completely unavailable for assimilation. The gaps are listed in Table S1 in the supporting information, and we exclude 10 which exceed 1° L_s in length from all of our analyses because the MACDA state within the gaps may or does depart considerably from that of the Martian atmosphere as portrayed in the rest of the data set. (An eleventh such gap occurs at the very end of MACDA, beyond the time span analyzed in this study, and is thus already excluded.) Examination of equatorial 0.5 hPa temperatures (not shown) suggests that some data gap-related distortions may persist beyond the ends of the intervals to be excluded; however, we expect the exclusions that are done to reduce any biases that would otherwise exist in our analyses.

Parts of our analysis compare seasonal means taken in different Mars years. Because data gaps are not the same across Mars years, the exclusion of such gaps from calculations of time means would result in each single-Mars year seasonal mean being taken over a somewhat different L_s range, potentially conflating real interannual variability with differences in observation availability. To avoid this problem, the L_s ranges associated with the 10 excluded data gaps are excluded from analysis in every Mars year, not just the Mars year in which TES observations were actually unavailable.

After completing most of the analyses presented here, we learned of a small offset between the L_s values provided as a time index in the MACDA data set and the actual astronomically correct L_s values that should be associated with each MACDA time step (L. Montabone, personal communication, 2015). In MY24 the MACDA L_s values are 0.128° too large, and the size of the offset is very similar in the other Mars years. Because we are concerned mainly with averages over seasons much longer than the size of the offset, we simply ignore this problem almost everywhere in this paper. However, the offset has been taken into account in the production of Figure 1 to appropriately synchronize the MACDA fields with TES dust opacity retrievals.

We use both pressure and sigma coordinates in our analysis. A constant sigma surface corresponds to a roughly fixed height above the surface, offers the advantage of never intersecting topography, and has been used in previous studies that examined low-level eddies [e.g., *Wang et al.*, 2013]. Unfortunately, the sigma coordinate lacks a readily accessible stream function-like quantity analogous to the geopotential height in a

Table 2. Pressure Levels (hPa) Used For Analysis

Hemisphere/Level	PRE	PAUSE	POST	SUMMER	DUST
NH p_{ref}	5.75	6.75	6.25	6	6.5
NH $0.9 \cdot p_{\mathrm{ref}}$	5.25	6	5.75	5.5	5.75
NH $0.5 \cdot p_{\mathrm{ref}}$	3	3.5	3.25	3	3.25
SH p_{ref}	4.75	4.5	4	4.75	4.75
SH $0.9 \cdot p_{\mathrm{ref}}$	4.25	4	3.5	4.25	4.25
SH $0.5 \cdot p_{\mathrm{ref}}$	2.5	2.25	2	2.5	2.5

pressure coordinate. However, the use of pressure coordinates for Martian atmospheric data analysis presents a challenge that is much less important on Earth: because of the substantial spatial variation in surface elevations and the large annual cycle in atmospheric mass on Mars, seasonal and interhemispheric variations of eddy activity on a given fixed pressure surface could simply reflect changes in the mean height of the pressure surface above the ground rather than changes in eddy activity at relatively fixed heights above the ground, which are dynamically more interesting.

Accordingly, for each hemisphere and season we have chosen a reference pressure level p_{ref} that is above ground for ~80% of the surface area poleward of 20° latitude in the hemisphere of interest. The pressure surface on which to analyze a given eddy field is then chosen to be (nominally) a particular fraction of the reference pressure, based on examination of plots of the zonal mean eddy fields as a function of latitude and pressure as described in section 4. For example, we analyze the eddy kinetic energy field at $0.5 \cdot p_{\mathrm{ref}}$. A list of all pressure levels used in this study is provided in Table 2. Although the chosen $0.5 \cdot p_{\mathrm{ref}}$ and $0.9 \cdot p_{\mathrm{ref}}$ levels are not exactly those fractions of p_{ref}, differences from the exact values are small: never more than 5.3%.

3. Eddy Zonal Wave Number Distributions

Although in section 1 we noted several disadvantages of decomposition into wave numbers as an approach to describing Martian transient eddies, to facilitate qualitative comparison of our results to previous work, we begin with a brief examination of the typical zonal scales of eddy activity in MACDA and the partitioning of eddy variance among zonal wave numbers. Figure 3 displays eddy wave number spectra based on temperature and meridional wind fields at $\sigma = 0.8996$. Wave number spectra are evaluated at one latitude for each season and hemisphere, chosen as the available latitude nearest the seasonal mean of the maximum in the zonal standard deviation of eddy temperature on $\sigma = 0.8996$.

The spectra are calculated by Fourier decomposing the field of interest $A(\lambda, t)$ in the zonal direction to get zonal wave number amplitudes $A(k, t)$ which are then squared and time averaged to yield the mean-squared amplitudes $\overline{A^2}(k)$ displayed in Figure 3. An interhemispheric difference in eddy strengths consistent with Figure 2 is apparent. Examining the temperature-based eddy spectra in detail first, we see that in the northern hemisphere they peak at wave number 2 for every Mars year and season of interest. In contrast, the southern hemisphere spectra peak at wave number 3 for six of the seven season-Mars year combinations plotted. Similar behavior is found for mean eddy wave numbers computed according to

$$\overline{k} = \frac{\sum_{k=1}^{36} k\overline{A^2}(k)}{\sum_{k=1}^{36} \overline{A^2}(k)} \tag{1}$$

In the southern hemisphere, PRE and POST seasonal mean $\overline{k}$ values never drop below 3.16, while northern hemisphere values for the same seasons never exceed 2.75. (The PAUSE $\overline{k}$ ranges for the two hemispheres overlap—see Table S2 for a complete listing of seasonal mean $\overline{k}$ values.)

Eddies based on meridional wind tend to be of larger zonal wave number than their temperature-based counterparts. For a given season, hemisphere, and Mars year, the peak of the meridional wind-based spectrum is located at or above the wave number at which the temperature-based spectrum peaks. Furthermore, for a given season and hemisphere meridional wind-based seasonal mean $\overline{k}$ values are invariably larger than those based on temperature. An interhemispheric difference in scales comparable to that for temperature-based eddies also occurs for meridional wind-based eddies. In the northern hemisphere the spectra peak at wave numbers 2 and 3, while in the southern hemisphere the peaks occur at wave numbers 3 and 4. Again the ranges of PRE and POST seasonal mean $\overline{k}$ values do not overlap between the two hemispheres: they never exceed 3.70 in the northern hemisphere or drop below 4.24 in the southern hemisphere.

Both seasonal and interannual variabilities are visible in the spectra. Weakening of the eddies during PAUSE relative to PRE and POST is quite evident, consistent with Figure 2. The global dust storm appears to have weakened northern hemisphere eddy activity, as pointed out by *Lewis et al.* [2007b]. Examining wave numbers 1 to 4, we see that the DUST spectra for storm-affected MY25 are weaker than those for the other two Mars years. This result carries over to PAUSE, but the storm-affected PRE eddies are only weakest at wave numbers 1 and 2. The eddies may also have shortened during the global dust storm: northern hemisphere seasonal mean $\overline{k}$ values for PRE, PAUSE, and DUST are consistently larger in MY25 than in MY24 and 26. This is qualitatively consistent with the eddy-scale response to increasing dust optical depths found in Mars GCM simulations by

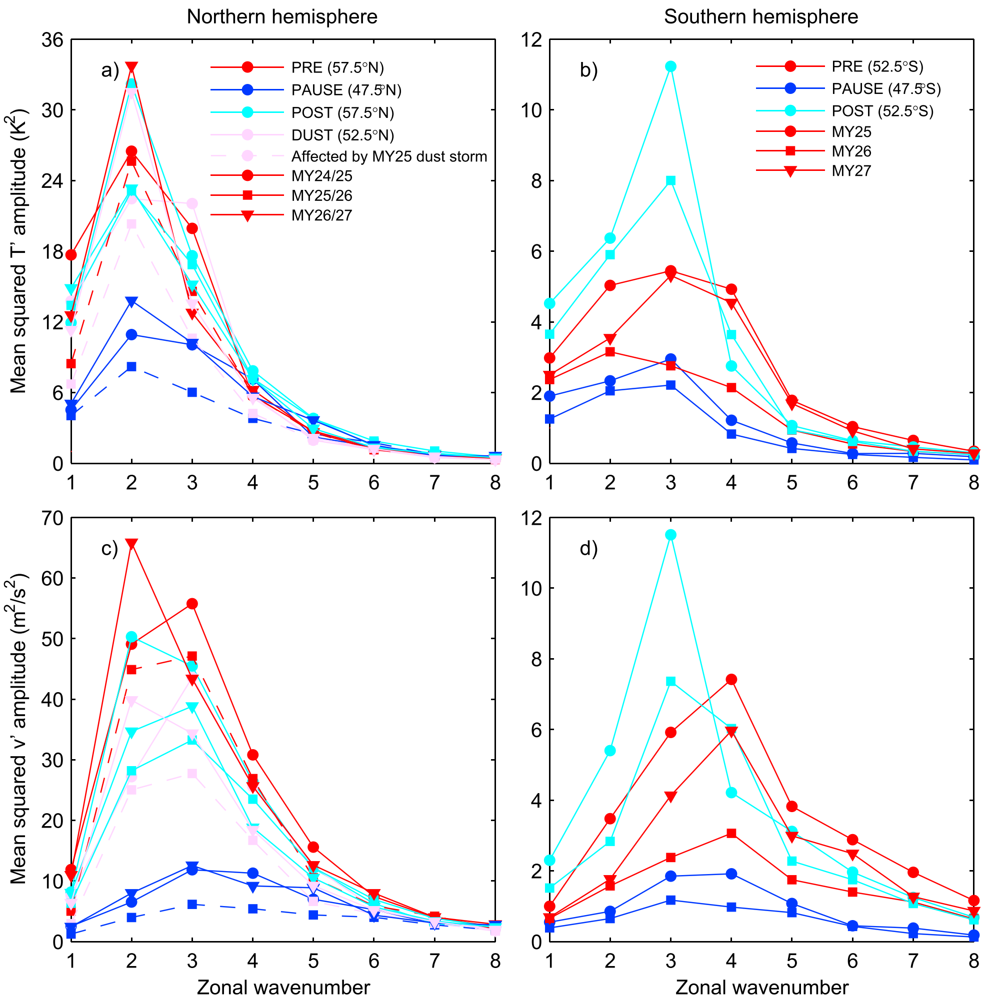

Figure 3. Plots of eddy zonal wave number spectra at $\sigma = 0.8996$ in MACDA. Figures 3a and 3b (Figures 3c and 3d) are derived from temperature (meridional wind) fields, while Figures 3a and 3c (Figures 3b and 3d) are for the northern (southern) hemisphere. Note the different vertical axis scales for the different hemispheres. Each spectrum is computed from a single season of data at the latitudes listed in the legend (see the main text for details on how these latitudes were selected). Line color denotes the season, the marker shape denotes the Mars year(s) from which the data came, and dashed lines indicate seasons significantly overlapping the MY25 global dust storm.

Barnes et al. [1993], although changes in the dominant zonal wave number as found by *Barnes et al.* [1993] are not evident in Figure 3. Finally, apparent interannual variability unrelated to the global dust storm is particularly prominent in southern hemisphere PRE. Whether the large interannual differences in eddy amplitude are real or merely a manifestation of time-dependent errors in the TES retrievals is unknown, and we leave this issue as a subject for future work.

The spectra presented here are most readily compared to those derived directly from TES observations by *Imamura and Kobayashi* [2009]. Their Figure 2 presents spectra for five 30° wide latitude bins as functions of season at 2.2 hPa. A substantial number of these spectra for the 45°–75°N latitude bin peak at wave number 1, in apparent contradiction to the results shown here. A similar discrepancy occurs in the southern hemisphere: some spectra that cover 45°–75°S and L_s ranges that intersect PAUSE and POST peak at wave number 2, and others intersecting PRE peak at wave number 1. Possible explanations of the difference include the substantially higher altitude considered by *Imamura and Kobayashi* [2009] (we estimate the altitude of 2.2 hPa to be ~12 km for 45°–75°N and ~7 km for 45°–75°S, much larger than the ~1 km of $\sigma = 0.8996$), their identification of transient eddies via a method that does not exclude slowly propagating upper level waves, and differences in the latitude ranges used to compute the spectra. Evidence for the first possibility is provided by repeating our spectral analysis on the 2.25 hPa surface. Temperature spectra at this level consistently peak at wave numbers the same as or lower than those at which their $\sigma = 0.8996$ counterparts peak.

It is more difficult to make comparisons to the extensive study of *Banfield et al.* [2004], who examine the vertical and meridional variation of eddy properties as a function of zonal wave number for wave numbers 1 to 3. The temperature spectra shown in Figure 3 of the present paper always peak at one of those wave numbers, but we find that the power at higher wave numbers is not necessarily negligible. Specifically, wave number 4 is prominent during southern hemisphere PRE but is also comparable to wave number 1 in amplitude during northern hemisphere PAUSE. This contrasts with *Banfield et al.* [2004], who evidently did not consider their wave number 4 results significant enough to present separately from those for other wave numbers. Curiously, it may also contrast with *Lewis et al.* [2007b], who described the first three wave numbers as "tend[ing] to dominate all higher wave numbers in the reanalysis record." This possible wave number 4 difference raises questions about the degree to which the TES retrievals actually constrain MACDA (and are able to portray Martian atmospheric behavior) at relatively short zonal scales, as well as the sensitivity of the results of spectral analyses to evaluation locations and other details. Our Fourier analysis of an assimilated data set may simply be a more effective method of detecting transient eddies than the techniques used by *Banfield et al.* [2004].

4. Variance-Covariance Fields

The spatial structure of transient eddy activity in the terrestrial atmosphere has often been characterized using maps of eddy variances and covariances [e.g., *Chang et al.*, 2002]. Although the maxima of such fields are often referred to as "storm tracks" in the terrestrial atmosphere literature, we avoid this term because it suggests that the transient eddies are in some sense confined or preferentially located within the storm tracks, which cannot be the case here, given the large zonal scale of the eddies as demonstrated in Figure 3. The Martian "storm tracks" are instead regions where eddies achieve relatively large amplitudes.

Four fields have been chosen for examination here: the eddy kinetic energy, a normalized RMS eddy geopotential height, the eddy meridional temperature transport, and the mean-squared eddy temperature. Using the $\overline{(\cdot)}$ operator to denote time averaging and $(\cdot)'$ to indicate the eddies, the eddy kinetic energy is

$$\mathrm{EKE} = \frac{1}{2}\left(\overline{u'^2} + \overline{v'^2}\right) \tag{2}$$

and the normalized RMS eddy geopotential height is

$$z'_{\mathrm{rms}N} = \left|\frac{\sin 60^\circ}{\sin\theta}\right| \sqrt{\overline{z'^2}} \tag{3}$$

where θ is the latitude and the prefactor has been applied to make $z'_{\mathrm{rms}N}$ more like a stream function [*Wallace et al.*, 1988]. The eddy meridional temperature transport and mean-squared eddy temperature are $\overline{v'T'}$ and $\overline{T'^2}$, respectively.

Plots of zonal mean interannual means of the eddy fields for each of the three major eddying seasons were used to help select appropriate levels for analysis of the eddy fields' horizontal structures. Eddy kinetic energy and RMS eddy geopotential height basically increase upward (to at least 0.1 hPa) at the latitudes of interest, so our choice to evaluate EKE and $z'_{\mathrm{rms}N}$ at $0.5 \cdot p_{\mathrm{ref}}$ is essentially arbitrary (albeit consistent with our desire to study relatively low-level waves). In contrast, the $\overline{v'T'}$ and $\overline{T'^2}$ fields have near-surface maxima that should be captured in an examination of horizontal structures. Our choice to evaluate these fields at $0.9 \cdot p_{\mathrm{ref}}$ achieves this goal and is presumably above ground to a greater extent than any higher-pressure surface would be.

In this section we summarize the climatological seasonal variation in eddy activity for each hemisphere separately, displaying maps of the interannual mean eddy fields for the three seasons that feature significant eddy activity. Since the MACDA data set is quite short by terrestrial standards (three Mars years each of northern hemisphere PRE, PAUSE, and POST and southern hemisphere PRE and two of southern hemisphere PAUSE and POST), to reduce the risk of overinterpreting weather noise in the interannual means, we separately examined maps for each Mars year individually and comment on them in the text. We then discuss the changes in eddy activity associated with the MY25 global dust storm and conclude the section with a comparison of the results to previous observational and modeling studies.

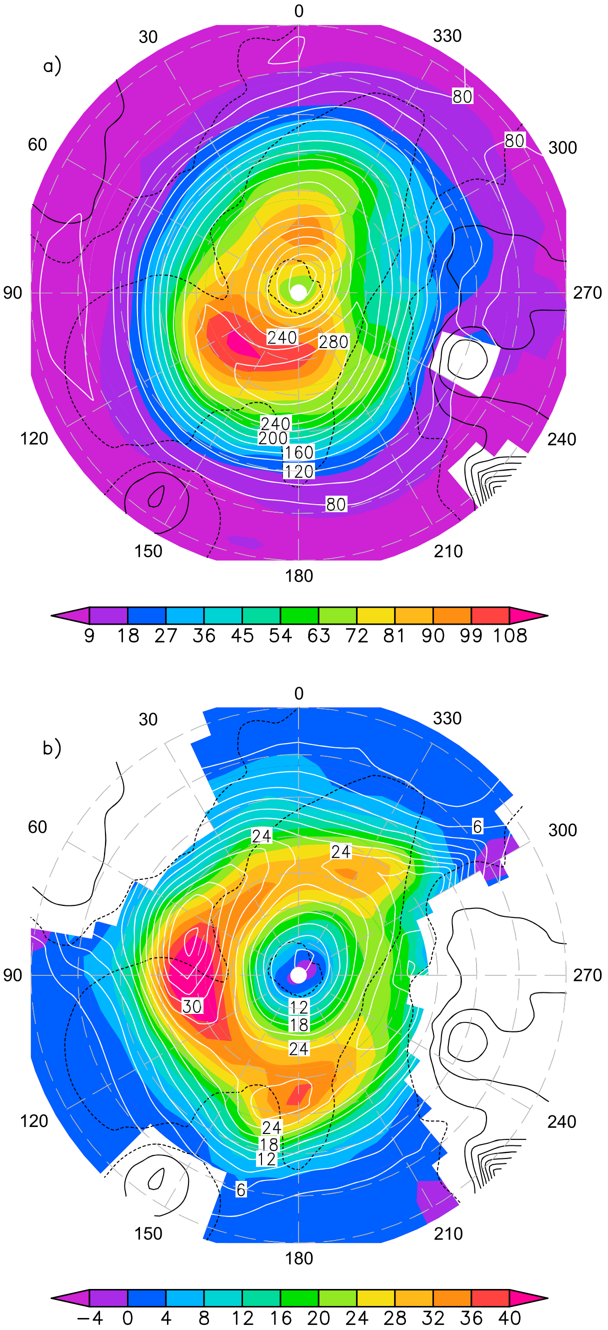

Figure 4. Interannual mean eddy fields for northern hemisphere PRE. (a) *EKE* fields (m^2 s^{-2}, shaded) and z'_{rmsN} (m, contoured) at $0.5 \cdot p_{\mathrm{ref}}$. (b) $\overline{v'T'}$ (K m s^{-1}, shaded) and $\overline{T'^2}$ (K^2, contoured). The projection is polar stereographic, with latitude lines spaced 10° apart and the most southerly line plotted at 20°N. Longitudes are labeled in degrees east. Topographic contours are spaced 2 km apart.

4.1. Northern Hemisphere Seasonal Cycle

The eddy variance-covariance maps for northern hemisphere PRE are shown in Figure 4. The interannual means were computed over all three available Mars years (24–26) and are thus influenced by the MY25 global dust storm. Examination of the fields for each Mars year individually demonstrates that the EKE field has a similar structure in all of them, with the most prominent local maximum extending over approximately 90°–210°E and a second local maximum located on the opposite side of the pole. In MY24 and 26, the $z'_{\mathrm{rms}N}$ field has its most prominent local maximum near 180°E, noticeably eastward of the EKE maximum. However,

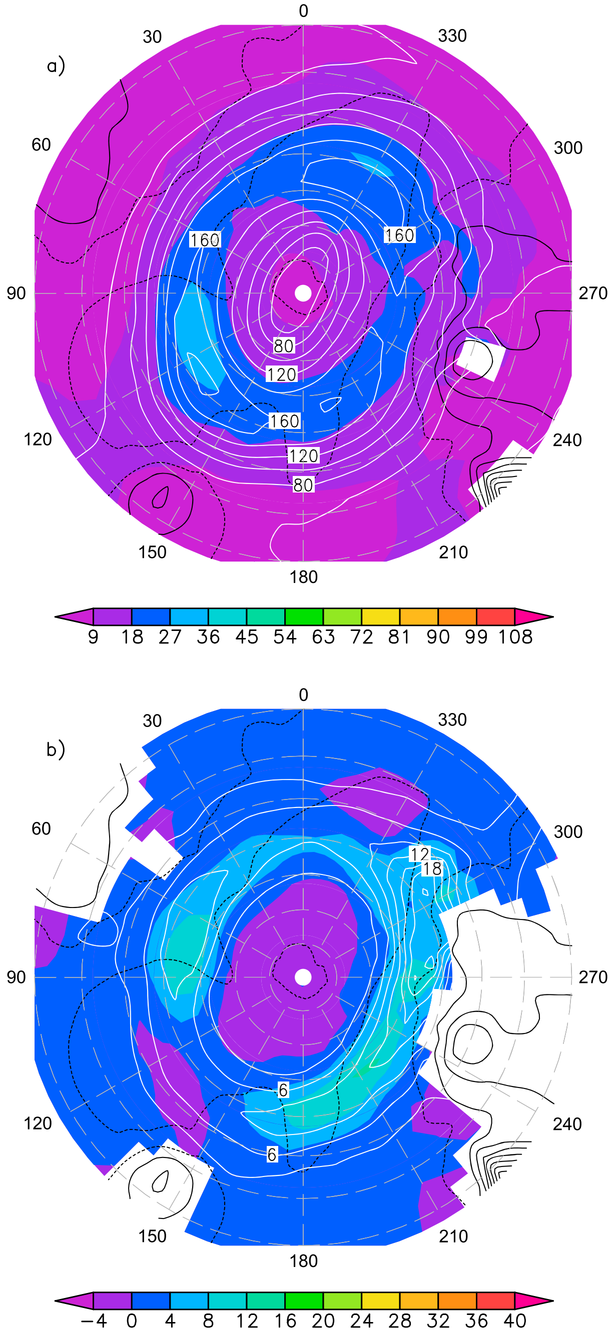

Figure 5. As in Figure 4 but for northern hemisphere PAUSE.

such zonal modulation is less prominent in MY25. Comparing both eddy fields to the topography, there may be a tendency for eddy activity to concentrate above low-lying areas.

Turning to the $0.9 \cdot p_{\mathrm{ref}}$ fields, the roughly wave number 3 pattern of $\overline{v'T'}$ is found in all three Mars years, with maxima near 90°, 180°, and 330°E. The $\overline{T'^2}$ fields bear some resemblance to the $\overline{v'T'}$ field, most notably in the presence of a $\overline{T'^2}$ maximum slightly west of the ~90°E $\overline{v'T'}$ maximum. Each of the three individual Mars year $\overline{T'^2}$ fields also features at least one other local maximum that is an analog of one of the $\overline{v'T'}$ maxima.

Figure 5 displays the eddy variance-covariance maps for northern hemisphere PAUSE, again averaged over MY24–26. An obvious reduction in EKE relative to what occurred during PRE is found in most regions—for

$>$ 88% of the area poleward of 20°N with defined values of the interannual mean, a tendency even more pronounced ($>$ 98% of the area) when consideration is restricted to poleward of 40°N. Qualitatively similar results are obtained when each Mars year is considered individually. $z'_{\mathrm{rms}N}$ drops over a large majority of the plotted region as well, both in the interannual mean and for each Mars year individually. None of this is surprising, as the season definitions were selected to concentrate the weakening of eddy activity near winter solstice into a single season. EKE local maxima peak near 120° and 330°E (again over low-lying areas) in at least MY24 and 26. The maxima were less clear in MY25, which was affected by the global dust storm, but all three Mars years possess $z'_{\mathrm{rms}N}$ maxima located similarly to the EKE maxima.

Consistent with the changes in eddy activity at $0.5 \cdot p_{\mathrm{ref}}$, the northern hemisphere PAUSE $\overline{v'T'}$ and $\overline{T'^2}$ fields have weakened in substantial majorities of the areas of interest–interannual mean values of $\overline{v'T'}$ were more strongly poleward and interannual mean values of $\overline{T'^2}$ were larger in PRE than in PAUSE over more than two thirds of the area with defined data north of 20°N. Overall both fields (particularly $\overline{v'T'}$) appear generally more zonal than their counterparts in PRE, with there nevertheless being two distinct regions of elevated eddy activity—approximately over 150°–330°E and 30°–120°E. An additional perspective on seasonal changes in all four eddy fields is provided by comparisons of area averages taken over all defined points poleward of 20°N, for each Mars year individually and as an interannual mean. All such means for PRE are found to be larger than all such means for PAUSE, consistent with the rest of the above analysis. This result also holds when the region of interest is restricted to poleward of 40°N.

The northern hemisphere POST eddy variance-covariance maps are displayed in Figure 6. The three Mars year interannual mean (MY24/25 to MY26/27) fields are not affected by the MY25 global dust storm. The EKE field's spatial structure is somewhat reminiscent of that for PRE, and as in PRE there may be some tendency for the most prominent $z'_{\mathrm{rms}N}$ maximum to be located downstream of the EKE maximum. However, the $z'_{\mathrm{rms}N}$ field seems relatively zonal in MY26/27. As in PRE, the $\overline{v'T'}$ field for northern hemisphere POST has an essentially wave number 3 pattern of maxima reasonably visible in every Mars year individually. The $\overline{T'^2}$ field bears some resemblance to the $\overline{v'T'}$ field, with one local maximum located near 60°E (slightly upstream of a $\overline{v'T'}$ maximum) and a second significantly more zonally extended maximum located north of Alba Mons (~250°E) that approximately overlaps the other two $\overline{v'T'}$ maxima. Eddy activity has clearly increased relative to PAUSE, with $\overline{v'T'}$ becoming increasingly poleward, in a substantial majority of the area poleward of 20°N for all four eddy fields in each of the three available Mars years. The change in eddy activity strength relative to PRE is less evident, with the year-to-year ranges of area-averaged eddy intensity for each season consistently overlapping for all four eddy fields and both the poleward of 20°N and poleward of 40°N regions. However, if the dust storm-affected MY25 PRE and MY25/26 POST from the same eddy season are excluded from consideration area-averaged EKE and $z'_{\mathrm{rms}N}$ are consistently larger in PRE than in POST (the ranges for $\overline{v'T'}$ and $\overline{T'^2}$ continue to overlap).

4.2. Southern Hemisphere Seasonal Cycle

Changing focus to the southern hemisphere, it is important to note that as mentioned in sections 2 and 3, southern hemisphere eddies are generally weaker than those found in the northern hemisphere. Accordingly, the color bars used to plot the EKE and $\overline{v'T'}$ fields have been changed. Figure 7 shows the eddy fields for PRE, averaged over MY25–27; the spatial structures of EKE and $z'_{\mathrm{rms}N}$ are seen to be broadly similar to each other and across Mars years. Both fields are characterized by a zonally extended maximum that begins at ∼150°E and continues to or beyond 330°E (basically south of the Tharsis bulge), and a second more localized maximum on the southern or southwestern rim of Hellas. The near-Hellas maximum is presumably a response to the local orography. The PRE $\overline{v'T'}$ and $\overline{T'^2}$ field spatial structures are also comparable to each other and across Mars years. Furthermore, they bear some resemblance to the $0.5 \cdot p_{\mathrm{ref}}$ eddy fields, with a zonally extended eddy activity maximum located roughly in the 150°–330°E hemisphere and a shorter maximum just upstream of Hellas.

Interannual strength variations of the eddy fields during PRE are consistent with those visible in the southern hemisphere panels of Figures 2 and 3. Area averaging over the region poleward of 20°S, values of EKE, $z'_{\mathrm{rms}N}$, and $\overline{T'^2}$ are consistently largest in MY25 and smallest in MY26. Similarly, $\overline{v'T'}$ is most strongly poleward in MY25 and most weakly poleward (in fact equatorward) in MY26. These results hold when the averaging region is restricted to poleward of 40°S as well, although $\overline{v'T'}$ in MY26 is no longer equatorward.

The spatial structures of southern hemisphere eddy fields during PAUSE, averaged over MY25–26, (Figure 8) appear similar to those of PRE. As expected given the way the season definitions were chosen, eddy activity

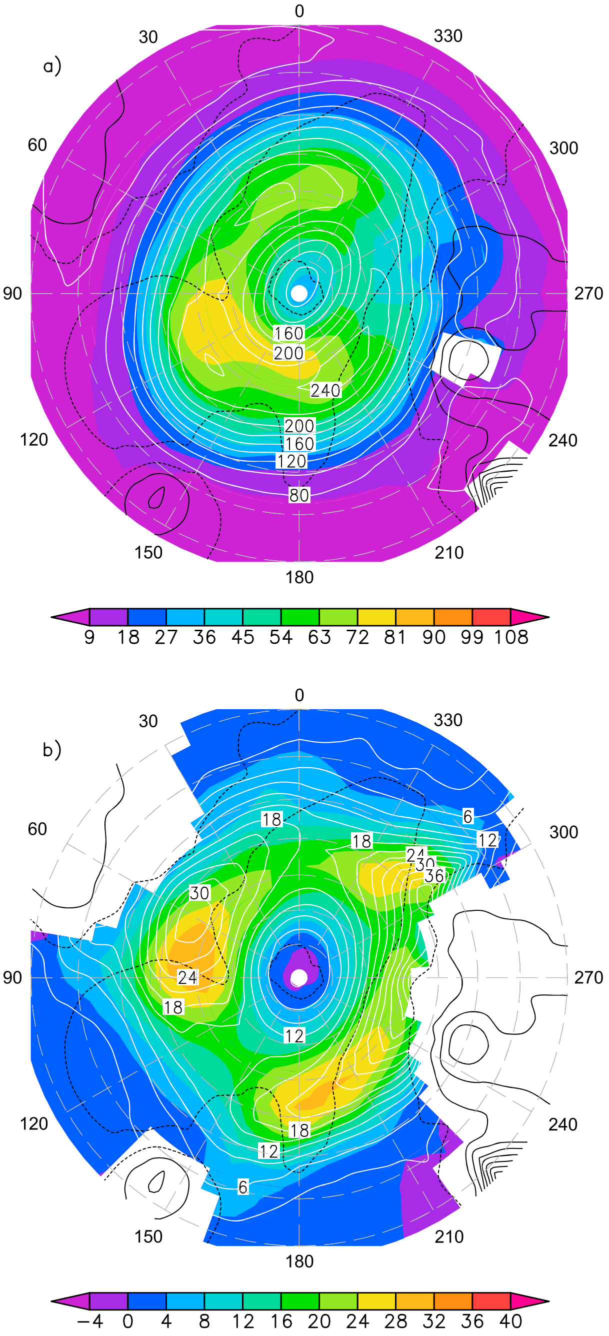

Figure 6. As in Figure 4 but for northern hemisphere POST.

tends to be weaker in PAUSE than in PRE: for each Mars year in which data for both seasons are available, EKE, $z'_{\mathrm{rms}N}$, and $\overline{T'^2}$ are larger in a majority of 20°–90°S during PRE than in the associated PAUSE. This result also holds for 40°–90°S and the interannual mean fields of both spatial averaging regions. Similar results are obtained based on comparisons of area averages of the same fields. Analyzing $\overline{v'T'}$ fields, it is found that $\overline{v'T'}$ is more poleward during PRE than PAUSE in majorities of both 20°–90°S and 40°–90°S for each relevant Mars year and in the interannual mean.

Finally, Figure 9 shows the southern hemisphere POST eddy fields, again averaged over MY25–26. The EKE and $z'_{\mathrm{rms}N}$ fields have spatial structures somewhat similar to those of PRE, with one local maximum associated with Hellas and another south of Tharsis. The Tharsis EKE maximum is most prominent in approximately 240°–300°E, and the associated $z'_{\mathrm{rms}N}$ may have a tendency to peak westward and equatorward of

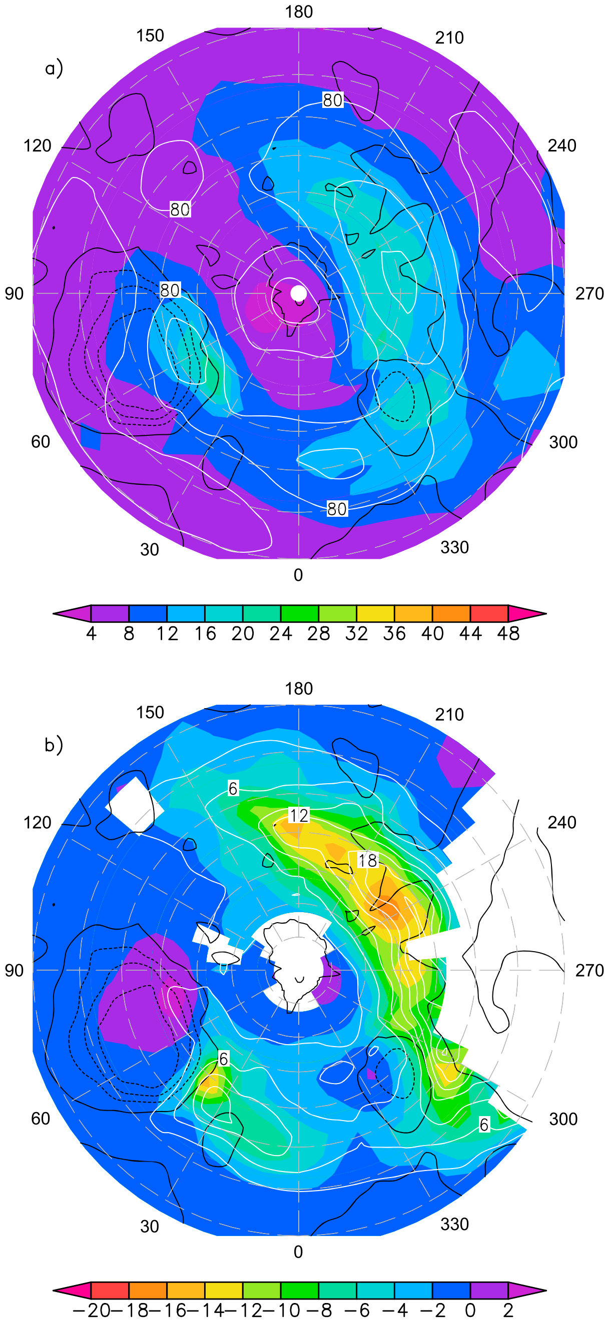

Figure 7. Similar to Figure 4 but for southern hemisphere PRE. Note the revised color bars for EKE and $\overline{v'T'}$. Again, the projection is polar stereographic, with latitude lines spaced 10° apart, longitudes labeled in degrees east and the most northerly line plotted at 20°S. Topographic contours are spaced 2 km apart.

the EKE peak. The $\overline{v'T'}$ and $\overline{T'^2}$ fields are again broadly similar to each other and are also quite similar to their counterparts in PRE, with one local maximum near Hellas and the other extended over approximately 150° – 330°E.

Unsurprisingly, the POST eddy activity is stronger than that of PAUSE: EKE, $z'_{\mathrm{rms}N}$, and $\overline{T'^2}$ are larger in POST than in PAUSE for vast majorities (> 98%) of the areas of interest (20° – 90°S and 40° – 90°S) in each Mars year individually and in the interannual mean, a result qualitatively consistent with the patterns of area averages of the same fields. Similarly to the results obtained comparing PRE and PAUSE, POST values of $\overline{v'T'}$ are more poleward than those of PAUSE for at least two thirds of both 20° – 90°S and 40° – 90°S in both available Mars

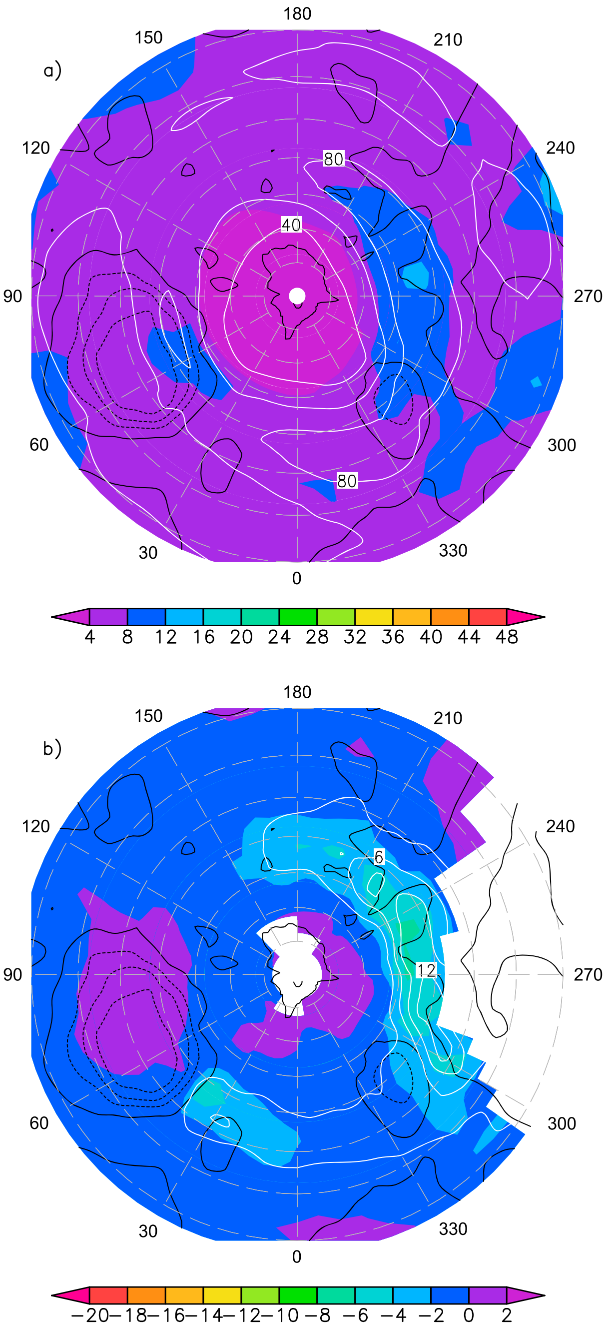

Figure 8. As in Figure 7 but for southern hemisphere PAUSE.

years and in the interannual mean. Less obviously, the POST eddy activity also tends to be stronger than that of PRE—all four eddy fields have larger (or in the case of $\overline{v'T'}$, more negative and thus more poleward) values in POST than in PRE for more than two thirds of each area of interest. This is true for each of the available Mars years individually and in the interannual mean. Again, comparisons of area averages of the eddy fields are consistent with this result as well.

4.3. Eddy Activity During the MY25 Global Dust Storm

The most prominent form of interannual variability in the Martian atmosphere is the global dust storm [*Smith*, 2008]. The MY25 global dust storm, which occurred over approximately L_s 186°–275°, significantly overlapped northern hemisphere PRE and PAUSE. To assess the relationship between the storm and eddy activity, we show in Figure 10 the four eddy fields averaged over the length of the MY25 global dust storm and

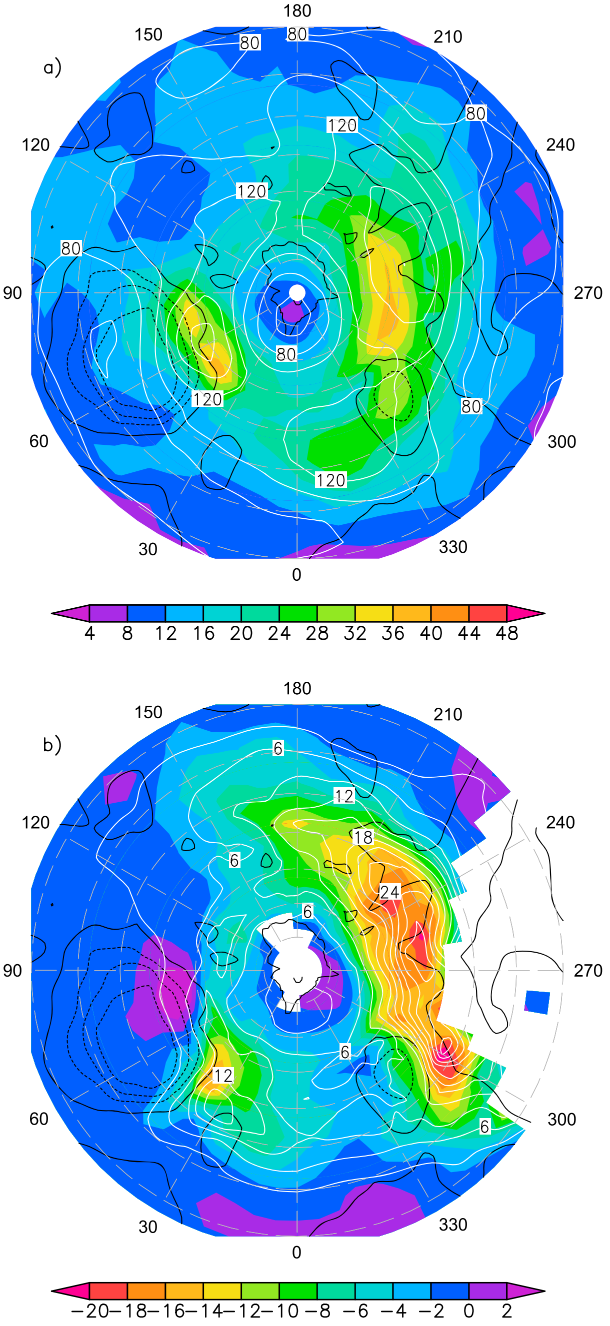

Figure 9. As in Figure 7 but for southern hemisphere POST.

averaged over the same L_s range in MY24 and 26. Overall, the storm seems to have had little impact on the spatial structures of the eddy fields; key local maxima present in the interannual mean over nondusty Mars years are still reasonably recognizable during the dust storm.

However, the amplitude of eddy activity was generally reduced: considering area means of the eddy fields over 20° – 90°N for each Mars year individually, it is found that all eddy fields but $\overline{T'^2}$ had their smallest area means in MY25. (All three area mean $\overline{v'T'}$ values were positive, so eddy temperature transport was most weakly poleward during the dust storm.) In contrast, area mean $\overline{T'^2}$ values consistently increased with increasing Mars year, although the MY25 values were closer to the lower MY24 values than to the higher MY26 values. All of these results hold when the eddy fields are averaged over 40° – 90°N as well. To some extent, this behavior

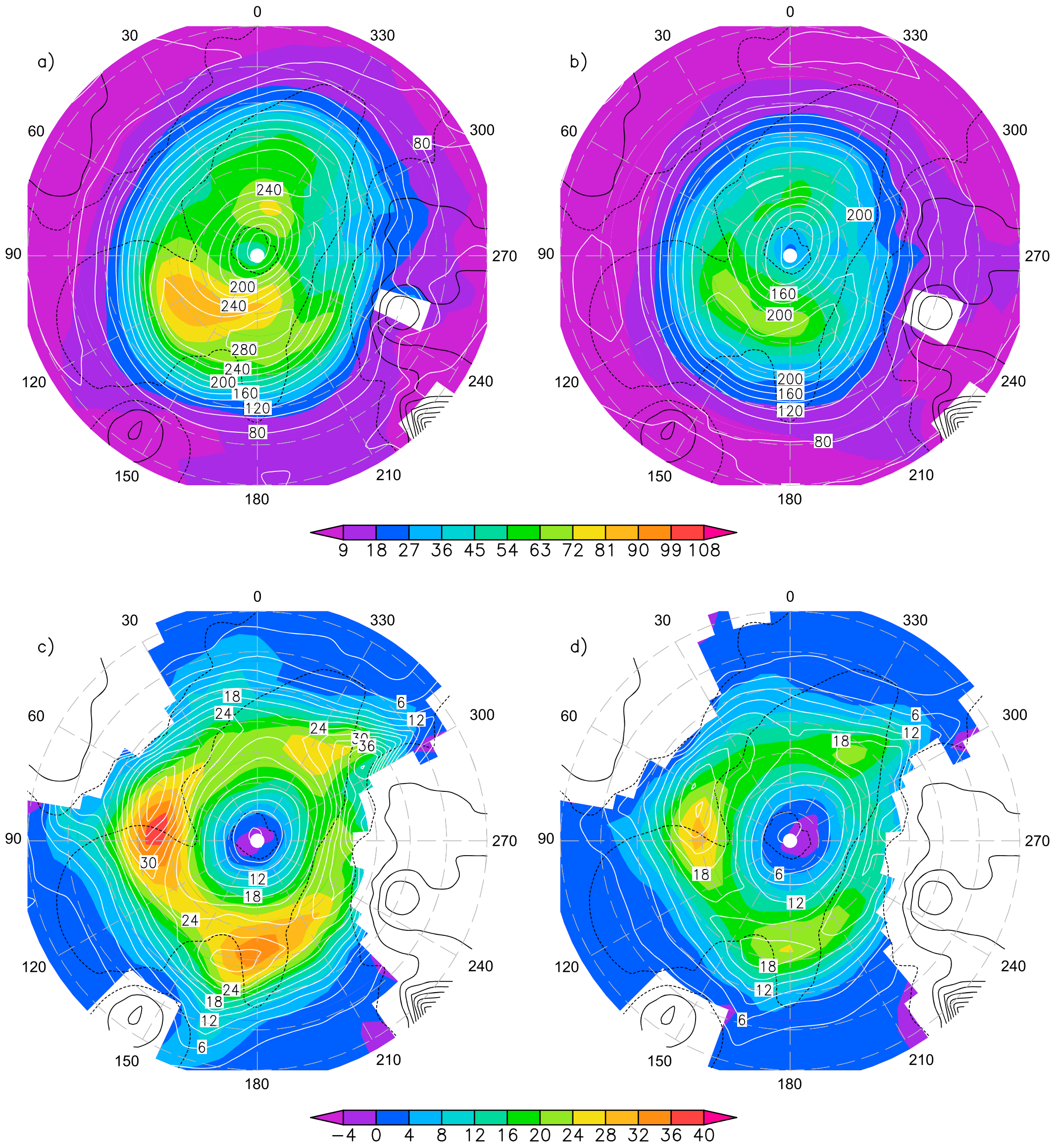

Figure 10. Similar to Figure 4 but for northern hemisphere DUST and with two columns to display (a and c) relatively clear (no global dust storm, average of MY24 and MY26 means) and (b and d) global dust storm (MY25) conditions.

contradicts the Mars GCM simulations of *Barnes et al.* [1993], who found that increasing the optical depth of a horizontally uniform dust field did not reduce eddy activity.

Because the MY25 global dust storm occurred largely during southern hemisphere SUMMER, its impact on southern hemisphere eddies will not be considered further here. It should also be noted that our assessment of the effect of the global dust storm on eddies does not address any impacts it may have had on lower frequency, higher-altitude waves [*Wilson et al.*, 2002; *Banfield et al.*, 2004] than are included in this study.

4.4. Comparison to Previous Observational and Modeling Studies

As a check on the robustness of the above results and a preliminary step toward the evaluation of Mars GCM eddy activity, we make comparisons to several earlier studies that assessed the horizontal structure of Martian transient eddy activity. *Lewis et al.* [2007b] examined a MACDA predecessor and *Banfield et al.* [2004] extracted the transient eddy component of the temperature field from TES retrievals directly, while *Hollingsworth et al.* [1996], *Basu et al.* [2006], and *Kavulich et al.* [2013] used the output of GCM simulations.

Figures 7 and 8 of *Lewis et al.* [2007b] display RMS eddy meridional wind velocities in the northern and southern hemisphere extratropics at 4 hPa for parts of MY24 and 26, respectively. This level is between 0.5 and

$0.9 \cdot p_{\mathrm{ref}}$ (but closer to the former) in the northern hemisphere and nearest $0.9 \cdot p_{\mathrm{ref}}$ in the southern hemisphere. Comparing to the EKE fields in Figures 4–6, 8, and 9 of the present paper, we see that the solstitial pause behavior is clearly present in the *Lewis et al.* [2007b] figures. Some similarities in the spatial patterns are visible as well; we expect that the differences are mainly indicators of the effect of the seasonal range, level, and/or exact variable used for the analysis.

Our comparisons to previous work emphasize studies using raw TES retrievals or free-running GCMs, as these analyses have more scope for differing from MACDA. The *Banfield et al.* [2004] results most comparable to the present work are contained in their Figures 19–20, which display results for the southern and northern hemispheres, respectively. Each of these figures is composed of maps of eddy temperature standard deviation computed over 12 30°-L_s months. The northern hemisphere results (Figure 20) are taken from MY25 and 26 and thus completely overlap the MACDA period (and contain the MY25 global dust storm), while the southern hemisphere results (Figure 19) overlap only MY25 PRE and part of PAUSE.

The *Banfield et al.* [2004] northern hemisphere eddies are mapped at 6.1 hPa, less than 1 hPa below the levels used to evaluate $\overline{T'^2}$ from MACDA. PRE is most comparable to *Banfield et al.* [2004]'s MY25 L_s 165°–195° and 195°–225° months. The spatial structures of eddy temperature differ significantly between the 2 months and although the local maximum in L_s 165°–195° is somewhat similarly located to a local maximum at ∼75°E in a plot of MY25 PRE $\overline{T'^2}$, a weakening from ∼90° to 150°E during L_s 195°–225° is not evident in MACDA. The *Banfield et al.* [2004] analysis clearly manifests the weakening of eddy activity near winter solstice that inspired the definition of PAUSE, and in L_s 285°–315° displays a local maximum analogous to the MY25 PAUSE $\overline{T'^2}$ maximum northeast of Alba Mons, although this maximum is insignificant in the two previous months. For MY25/26 POST, the wave number 2 pattern of MACDA $\overline{T'^2}$ may be captured best in *Banfield et al.* [2004]'s MY25 L_s 315°–345° but has faded conspicuously by MY26 L_s 15°–45°.

In the southern hemisphere *Banfield et al.* [2004] mapped eddy activity at 3.7 hPa, between $0.5 \cdot p_{\mathrm{ref}}$ and $0.9 \cdot p_{\mathrm{ref}}$ but closer to the latter. The region of high-latitude eddy activity (poleward of 70°S) present during MY24 L_s 345°–MY25 L_s 15° according to *Banfield et al.* [2004] is not evident in MACDA MY25 PRE $\overline{T'^2}$. However, the tendency for eddy temperatures to peak south of Tharsis during MY25 L_s 15°–45° and L_s 45°–75° is shared with MACDA MY25 PRE. *Banfield et al.* [2004]'s plots contain a manifestation of the solstitial pause, with clearly weaker eddy activity in MY25 L_s 75°–105° than in L_s 45°–75° or in MY24 L_s 105°–135°. Finally, MY24 L_s 105°–135°, L_s 135°–165°, and L_s 165°–195° all exhibit maxima south of Tharsis, as found in MACDA PAUSE and POST. The latter two months also show some evidence of sharing a local maximum near Hellas with MACDA POST.

The GCM study most directly related to the present work is *Hollingsworth et al.* [1996], who used the *Pollack et al.* [1990] version of the Ames Mars GCM to study the spatial structure of transient eddy fields in the northern hemisphere winter solstice (L_s 270°) circulation. EKE and $\overline{v'T'}$ fields at 5 hPa are displayed in their Figures 1 and 2, respectively. This season is most comparable to PAUSE in the present paper, with the level chosen for analysis in *Hollingsworth et al.* [1996] between those used here for EKE and $\overline{v'T'}$. Although direct comparison of *Hollingsworth et al.* [1996] to the PAUSE results shown in Figure 5 is complicated by a lack of detail, a different version of the figure with the color bars spanning a narrower range indicates that the MACDA interannual mean PAUSE EKE field does have three prominent local maxima in longitude ranges similar to those of the *Hollingsworth et al.* [1996] simulation. However, the relative strengths of the various maxima differ between MACDA and the simulation. Reasonable agreement in the spatial structures of the *Hollingsworth et al.* [1996] and MACDA $\overline{v'T'}$ fields is also found, with a zonally extended maximum in both fields extending over ∼180°–330°E. A second local maximum in the opposite hemisphere is also present in both MACDA and the *Hollingsworth et al.* [1996] simulation, although the exact longitude of the peak may differ by ∼45°.

Basu et al. [2006] used the *Basu et al.* [2004] version of the Geophysical Fluid Dynamics Laboratory (GFDL) Mars GCM to study global dust storms and presented low-level (2 km above ground) $\sqrt{\overline{v'^2}}$ fields at six L_s values ranging from 195° to 345° in their Figure 18. The most evident similarity to the MACDA results shown here is the presence of a solstitial pause. The connection between the topography and spatial distribution of eddy activity seems clearer than in the MACDA EKE fields, perhaps because $0.5 \cdot p_{\mathrm{ref}}$ is typically ∼8 km above ground and thus less directly affected by it. Finally, *Kavulich et al.* [2013] examined several aspects of baroclinic waves in a more recent version of the GFDL Mars GCM and exhibit a vertically averaged EKE field in their Figure 11. Their results are most comparable to the single-level PRE EKE field in Figure 4 and the spatial patterns are in

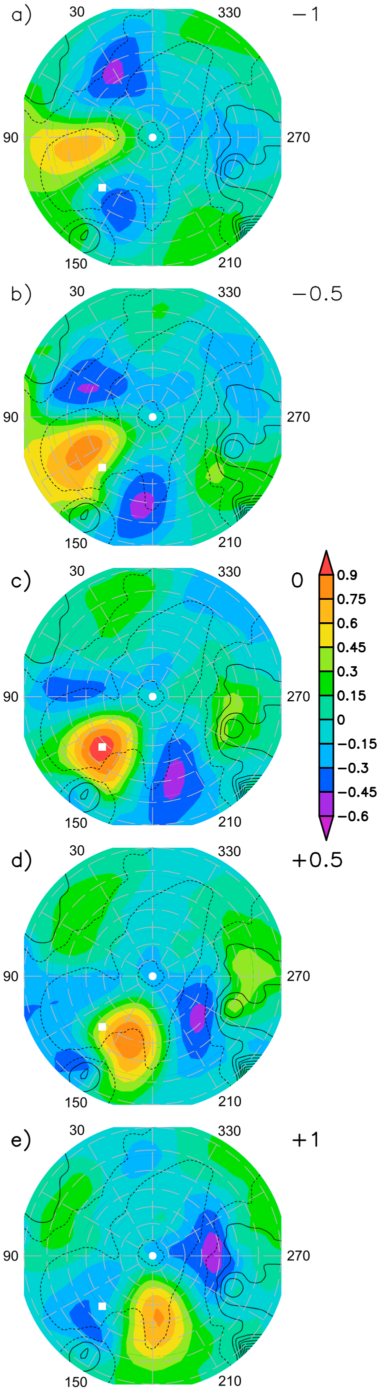

Figure 11. Teleconnection maps of the eddy surface pressure field, computed over all three available Mars years of northern hemisphere POST. The reference point (47.5°N, 135°E) is marked with a white square. The number in the upper right corner of each panel is the lag (in sols) used to compute the teleconnection map. Map projection, latitude and longitude lines, and topographic contours are as in Figure 4.

good agreement, particularly in the position of the absolute maximum and in the tendency for relatively weak eddy activity north of Alba Mons.

5. Eddy Phase Velocity Fields

The results shown in section 4 present an essentially Eulerian view of the transient eddies, in that Figures 4–10 depict eddy activity as a form of time dependence of the atmospheric state at fixed spatial locations. However, the eddy activity clearly occurs as coherently traveling weather systems, a fact not captured by the above analysis. This limitation could be addressed by adopting a more Lagrangian perspective, systematically tracking individual cyclones and anticyclones [e.g., *Hoskins and Hodges*, 2002]. Here we have opted to take a hybrid approach, defining and characterizing eddy structures and propagation characteristics via teleconnection maps [e.g., *Wallace et al.*, 1988].

The concept of teleconnection has seen little previous use in Martian atmospheric studies [*Martínez-Alvarado et al.*, 2009; *Kavulich et al.*, 2013], and the term itself has been applied to a number of related but distinct analysis techniques. Accordingly, an introduction to our specific method is in order. We define our teleconnection maps after *Wallace et al.* [1988], by first choosing a field for analysis (eddy surface pressure or eddy geopotential height in this study), a time interval (one of the major eddy seasons), and a reference point. We then compute and map the correlation over the time interval of interest between the time series of the field at the reference point (the reference series) and the time series of data for every point in the field, revealing a typical spatial structure of whatever time variability is present in the data set in the vicinity of the reference point. It is also possible to create teleconnection maps after having shifted the reference series in time relative to the field time series; for example, given a total of N time steps of data a teleconnection map for which time steps 1 to $N-1$ of the reference series were correlated with steps 2 to N of the field time series would be said to have lag +1. Comparison of teleconnection maps at several lags can reveal propagation of eddies.

We illustrate these ideas in Figure 11. Five teleconnection maps based on the eddy surface pressure field are shown for lags from −1 to +1 sol, with the reference point (47.5°N, 135°E) chosen as the MACDA grid point nearest the Viking 2 landing site. This range of lags is sufficiently large to clearly demonstrate evolution of the teleconnection pattern, while remaining small enough for changes between individual panels of the figure to be fairly smooth. The correlation maximum moves eastward with increasing lag, indicative of eastward propagating transient eddies with periods of roughly 2 to 4 sols. Correlation minima upstream and downstream of the primary maximum are visible and propagate as well. Their number and spacing show the eddies to have a typical wave number of ~3. Previous observations and simulations of low-level transient waves exhibit wave periods in the 2 to 3 sol range for wave number 3 and in the 3 to 4 sol range for wave number 2 [*Barnes et al.*, 1993; *Wilson et al.*, 2002; *Wang et al.*, 2003; *Banfield et al.*, 2004; *Basu et al.*, 2006], although it must be noted that wave number and period estimates made using teleconnection maps are quite crude because they essentially average over all wave numbers and any seasonal variations in the periods and amplitudes of individual wave numbers. Such seasonal variations may be substantial, given that the season used (northern hemisphere POST) extends over 115° L_s. The maps further suggest that the eddies may deform around topography; note the behavior of the primary maximum near Elysium Mons (~150°E) and the downstream minimum north and west of Alba Mons. Some evidence of such behavior is also found in the instantaneous eddy surface pressure fields shown in Figure 18 of *Kavulich et al.* [2013].

Lagged teleconnection maps such as those shown in Figure 11 suggest a way to estimate a phase velocity at their reference points: compute the position of the primary maximum as a function of time (lag) and estimate the velocity by using a finite-difference approximation to the derivative [*Wallace et al.*, 1988]. We implement this idea by computing teleconnection maps with lags ±0.5 sols for all points in our regions of interest, then for each map identify the distance and direction from the reference point to the maximally correlated point. Each distance and direction pair is converted to a velocity by dividing by the lag, and the two velocity values are averaged together to yield the final velocity estimate. The chosen ±0.5 sol lags should be suitable for this purpose because, assuming eddy zonal phase speeds of $\sim60°$ sol^{-1} (as would occur for wave number 3 with a 2 sol period), the correlation maxima on the lagged teleconnection maps should be located ~30° from their reference points. This distance is small enough for the phase velocity estimate to remain fairly local, while being large enough to contain multiple MACDA grid boxes and thus limit artificial quantization of the phase speeds caused by MACDA's finite resolution.

Figure 12 shows the mean eddy phase velocity field for northern hemisphere POST, averaged over all three available Mars years. Arrows show phase velocity vectors computed as described above, while the shading indicates the propagation direction. Eddies are defined using $0.5 \cdot p_{\mathrm{ref}}$ geopotential height and surface pressure for Figures 12a and 12b, respectively. The most striking feature of the phase velocity fields is an apparent tendency of eddies to propagate in the general direction of topographic contours, a behavior most evident near Alba Mons. Four regions of relatively prominent topography-following behavior are outlined in purple in each panel of the figure. This tendency is apparently stronger at the surface than at $0.5 \cdot p_{\mathrm{ref}}$: compare the intensities of the shadings in the four outlined regions. Note that the region of strong southeastward eddy propagation to the east of Alba Mons partly intersects Acidalia Planitia, which has been identified as the most prominent source of flushing dust storms [*Hinson and Wang*, 2010; *Wang and Richardson*, 2015] and in which the example storm presented in Figure 1 was located.

The results shown in Figure 12 are highly robust, which is why a figure for only one northern hemisphere season is shown. When area-averaged eddy phase velocities are computed over each of the outlined regions for every available combination of season, Mars year, and level (4 regions × 3 seasons × 3 Mars years × 2 levels) the meridional component of the phase velocity is in the direction consistent with the topography—north for the regions centered at 205°E and 15°E, south for those centered at 300°E and 80°E. Furthermore, in nearly all cases (35 of 36—the exception is MY24 PAUSE in the 80°E region) the direction of eddy propagation is more meridional at the surface than at $0.5 \cdot p_{\mathrm{ref}}$. Finally, the interannual range of surface eddy propagation directions for each region and season overlaps the ranges for the other two seasons; this suggests that any seasonal cycle of eddy propagation directions is relatively insignificant, at least at the surface and within the outlined regions of interest.

It is reasonable to compare eddy phase velocities based on eddy geopotential heights and eddy surface pressures because both fields are stream function-like. This is obvious for the eddy geopotential height field but merits more discussion in the case of the eddy surface pressure field. Using the primitive equations in an arbitrary vertical coordinate [e.g., *Durran*, 2010, equation (8.100)] and the definition of sigma coordinates, we can show that geostrophic balance in sigma coordinates is

$$f\hat{z} \times \vec{u}_g = -\frac{\sigma}{\rho}\nabla p_s - g\nabla_\sigma z \tag{4}$$

where f is the Coriolis parameter, $\hat{z}$ is the vertical unit vector, $\vec{u}_g$ is the geostrophic velocity, ρ is the density, g is the gravity, and z is the geopotential height. The subscript σ denotes evaluation of the horizontal derivative on a surface of constant sigma. At the surface ($\sigma = 1$), $z = z_s$ where z_s is the geopotential height of the topography. Because z_s is time-independent, filtering equation (4) to extract the transient eddies eliminates the second term on the right-hand side. The relationship between $\vec{u}_g$ at the surface and p_s is thus analogous to the relationship between $\vec{u}_g$ on a pressure surface in the free atmosphere and z on the same pressure surface, assuming that variations in ρ at the surface are negligible.

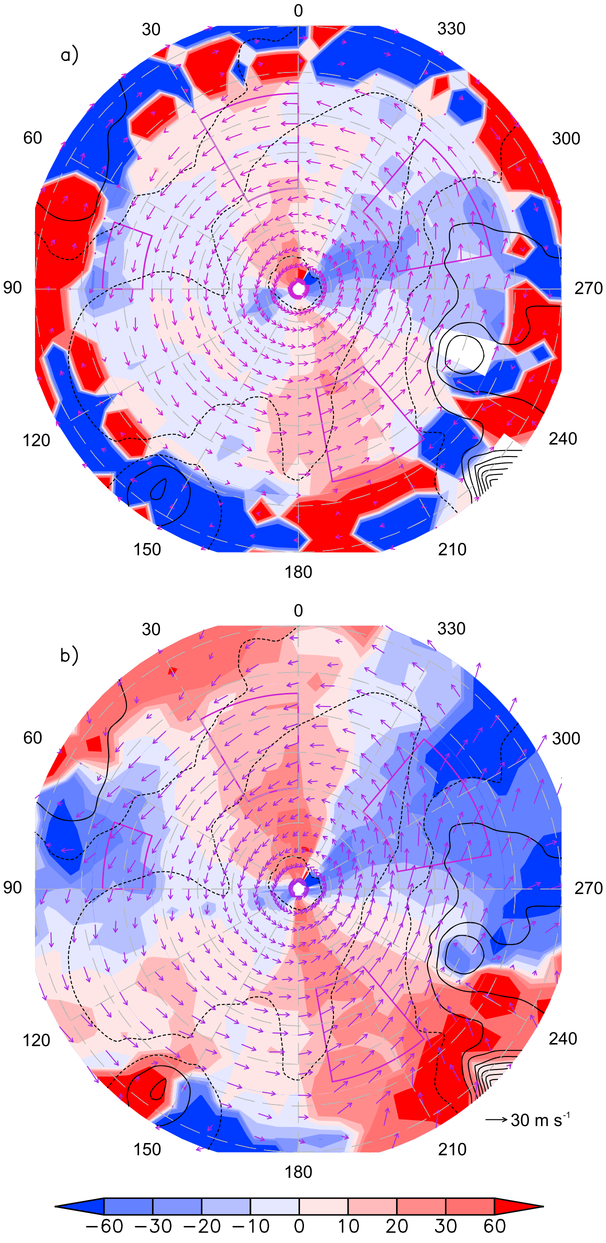

Figure 12. Interannual mean eddy phase velocity information for northern hemisphere POST. Arrows indicate the phase velocities (m s^{-1}, see scale arrow), while the shading indicates the propagation direction (degrees measured counterclockwise from due east). (a and b) Based on the $0.5 \cdot p_{ref}$ geopotential height field and the surface pressure field, respectively. Four regions of prominent nonzonal eddy propagation have been outlined in purple. Map projection, latitude and longitude lines, and topographic contours are as in Figure 4.

To address the possibility that the above argument is invalidated by large variations in ρ or other unanticipated factors, we also assessed the degree of surface trapping of meridional propagation using only eddy geopotential heights on pressure surfaces. We computed area-averaged eddy phase velocities for the outlined regions on the physically lowest (highest pressure) pressure surfaces we deemed usable (i.e., were above ground sufficiently often). The selected pressure surfaces were region and season specific, and for three of the four regions were located at $> 0.95 \cdot p_{\text{ref}}$ in each of the three major eddying seasons. (The exception was the 300°E region, for which the lowest usable pressure surfaces varied from 0.70 to $0.74 \cdot p_{\text{ref}}$). This analysis confirmed the surface pressure-based result on surface trapping of the meridional propagation; specifically, for every season-Mars year-region combination except MY24 PAUSE in the 80°E region, eddies propagated more meridionally (and in the expected directions) at very low levels than they did at $0.5 \cdot p_{\text{ref}}$.

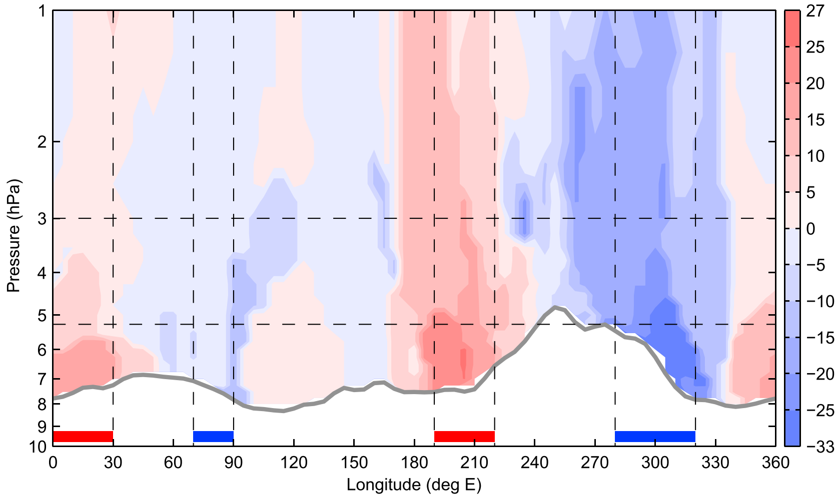

Figure 13. Vertical section of interannual mean eddy phase propagation directions at 47.5°N for northern hemisphere PRE. The shading shows the propagation direction (degrees counterclockwise from due east), while vertical black dashed lines and red and blue solid lines at the bottom of the plot indicate the zonal extents of the regions of interest outlined in Figure 12. The gray solid line indicates the time mean surface pressure, while the horizontal black dashed lines mark the $0.5 \cdot p_{\mathrm{ref}}$ and $0.9 \cdot p_{\mathrm{ref}}$ pressure surfaces.

The surface trapping of meridional eddy propagation is also frequently visible in vertical sections of eddy phase propagation direction, calculated from geopotential heights on pressure surfaces at 47.5°N. A representative sample is displayed as Figure 13, an interannual mean for PRE averaged over all three available Mars years. The longitude ranges of the four regions of interest are marked by vertical lines and horizontal colored bars, and propagation directions are clearly more meridional near the surface for all but the 80°E region (note though that this region as identified in Figure 12 extends only to 45°N). Similar features are seen in sections calculated for individual season-Mars year combinations: surface trapping of meridional propagation is seen for all nine combinations of major eddying seasons and available Mars years for the 205°E and 300°E regions and seven of the combinations for the 15°E region but for only four combinations for the 80°E region.

Southern hemisphere eddy phase velocity results are shown in Figure 14, as an interannual mean over MY25–27 for PRE. A region of topography-following behavior is outlined on the southeastern flank of Tharsis. Again, the area-averaged eddy phase velocity in the region always (for both levels and all seven available combinations of season and Mars year) has a northward component consistent with the topography and the eddy propagation direction is more meridional at the surface than at $0.5 \cdot p_{\mathrm{ref}}$. As for the northern hemisphere, near-surface eddy propagation directions were also assessed using low-level pressure surfaces (0.84 to $0.89 \cdot p_{\mathrm{ref}}$, depending on the season), confirming the surface trapping of meridional propagation found using surface pressure-based eddies. Although the interannual range of PAUSE surface pressure eddy propagation directions does not overlap those of PRE or POST, the range across all seven season-Mars year combinations of eddy propagation directions (measured counterclockwise from due east) is just 30.6° to 33.6°—quite small relative to the typical scale of the departure from zonal propagation.

Another interesting form of terrain-following eddy propagation is visible at the surface in the Hellas region, in which eddies move cyclonically along the slopes of the basin. This behavior is visible for all available combinations of seasons and Mars years but is not reproduced at $0.5 \cdot p_{\mathrm{ref}}$, in qualitative agreement with the surface trapping of terrain-following behavior documented for the other five outlined regions. We leave a more complete characterization of eddy propagation in and near Hellas as a subject for future work.

Finally, some of the eddy phase velocity vectors shown in Figure 14a serve to highlight a caveat that must be attached to the analyses presented here. Near 22.5°S, 240°E there are several vectors indicating velocities much larger than those at nearby points. Such nonsmoothness of the eddy phase velocity field seems physically implausible, suggesting that our phase velocity calculation algorithm is producing a misleading result. Examples of this phenomenon are not uncommon in seasonal phase velocity maps for individual Mars years, and some are more extreme than illustrated here. However, the general smoothness and overall physical

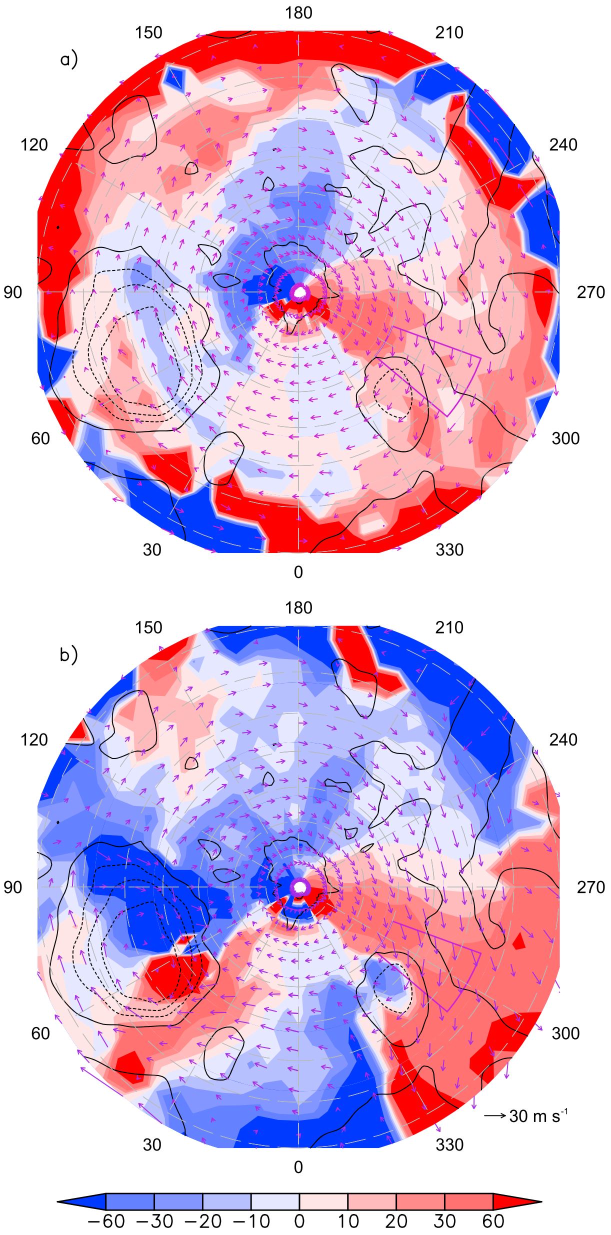

Figure 14. As in Figure 12 but for southern hemisphere PRE. Only one region of nonzonal eddy propagation is outlined, but note the pattern of cyclonic eddy propagation at the surface in the Hellas region. Map projection, latitude and longitude lines, and topographic contours are as in Figure 7.

reasonableness of the results we obtain nevertheless strongly suggest that the diagnostic is sufficiently reliable to be useful.

6. Discussion

As yet we have said little about the physical causes of the documented eddy behaviors. There have been several studies of linear baroclinic instability in the Martian atmosphere, the most recent and sophisticated of which are *Barnes* [1984], *Barnes et al.* [1993], and *Tanaka and Arai* [1999]. Differences between the methodologies of these studies and those of the present work would make a detailed comparison difficult, and it is not immediately obvious which metric of MACDA transient eddy scale is most appropriate for comparison to the results of a linear instability analysis—for example, variation of the vertical structure of eddies with zonal wave number [e.g., *Banfield et al.*, 2004] should cause observationally-based wave number spectra to vary with altitude. However, it is interesting to note that while instability was maximized at wave numbers 3 and 4 for realistic basic states in *Barnes* [1984] and *Barnes et al.* [1993] and at wave numbers 5 and 6 in *Tanaka and Arai* [1999], temperature-based eddy spectra at $\sigma = 0.8996$ always peak at wave numbers 2 and 3 and mean wave numbers for individual seasons, hemispheres, and Mars years never exceed 3.60 (Table S2). Agreement with linear instability analyses is better for eddy scales based on meridional wind: the spectra peak at wave numbers 2 to 4 (Figure 3) and mean wave numbers range from 3.29 to 5.32 depending on the season, hemisphere, and Mars year (Table S2). It is clear that the most linearly unstable baroclinic waves on Mars-like basic states have wave numbers that are within a factor of a few of the wave numbers of the nonlinear eddies in MACDA, but this level of agreement is too coarse to be very informative. To fully assess the degree to which linear baroclinic instability explains (or fails to explain) Martian transient eddy scales, it may be useful to conduct more systematic studies comparing linearly unstable waves and nonlinear eddies associated with exactly the same basic states [e.g., *Merlis and Schneider*, 2009].

In section 4.4 we reported that the EKE and $\overline{v'T'}$ fields of a Mars GCM simulation described in *Hollingsworth et al.* [1996] were comparable to those derived for a similar level and season of MACDA. *Hollingsworth et al.* [1996] found that the topography was key to the spatial pattern of eddy activity in their model, based on a comparison to a simulation without topography, and argued for the effect of meridional slopes on baroclinic instability as an underlying mechanism [*Blumsack and Gierasch*, 1972]. Although more detailed comparisons between MACDA and free-running Mars GCM simulations are needed and the *Hollingsworth et al.* [1996] theoretical arguments could be elaborated upon, the northern hemisphere analysis presented here is consistent with their overall results.

Finally, topography-following disturbances were detected in the terrestrial atmosphere by *Hsu* [1987] and, for most of the cases analyzed, were identified as topographic Rossby waves. Topographic Rossby waves propagate anticyclonically around raised topography and should be surface trapped in a baroclinic atmosphere [*Hsu*, 1987]. This is in agreement with the results presented in section 5, although further work is needed to confirm such an identification.

This study has largely accepted MACDA at face value as a reasonable representation of the Martian atmosphere, including for fields not assimilated. *Montabone et al.* [2006] demonstrated that a preliminary version of the MACDA data set generally agreed better with radio occultation-based temperature profiles than did the UK Mars GCM run without data assimilation, suggesting that the assimilation did in some sense work (albeit with demonstrable biases during the MY25 global dust storm and in northern middle-high latitudes). Furthermore, as discussed in section 1 assimilation of temperature data creates MACDA's northern hemisphere solstitial pause, indicating that at a minimum the data assimilation profoundly affects the data set's transient eddy activity.

The ability of the assimilation algorithm underlying MACDA to accurately represent transient eddies has been assessed in several studies using simulated observations [*Lewis and Read*, 1995; *Lewis et al.*, 1996, 1997]. Positive results were obtained for the reproduction of the amplitude and phase of wave number 3 in a flow where it was strong [*Lewis et al.*, 1996] and for surface pressure at the Viking 2 landing site [*Lewis et al.*, 1997]. However, *Lewis et al.* [1996] also reported that the assimilation of only temperature data resulted in production of a spurious barotropic wave component in their idealized GCM, leading to large surface pressure errors. Additionally, using an ensemble Kalman filter-based data assimilation system *Greybush et al.* [2012] showed significant sensitivity of a sample instantaneous low-level eddy field to the assumed dust scenario and other physics details of the underlying GFDL Mars GCM. In any case, it is not clear how to extrapolate such results to all of the variables and diagnostic techniques used here and so there is no obvious way to estimate the accuracy of the final results.

7. Conclusion

We have presented an extensive study of Martian transient eddies based on the MACDA reanalysis. Since data assimilation can be used to estimate atmospheric fields not directly retrievable from TES profiles, we are able to examine quantities other than temperature much more readily than previous studies could. Because atmospheric dynamical theories are generally not cast solely in terms of temperature, MACDA and other Mars reanalyses hold promise as more physically interpretable pictures of the Martian atmosphere than raw spacecraft observations are.

This study emphasizes the spatial distribution and spatially localized propagation characteristics of Martian transient eddies, topics which have received fairly limited attention in previous works. Because of strong% seasonality in characteristic eddy amplitudes and latitudes, we subdivided the Martian year into four seasons (three of which produce substantial eddy activity) for analysis purposes. While this seasonal subdivision may be relatively coarse [cf. *Banfield et al.*, 2004; *Lewis et al.*, 2007b], it does clearly capture the drop in eddy activity that occurs near each hemisphere's winter solstice. We considered four transient eddy fields (EKE, $z'_{\mathrm{rms}N}$, $\overline{v'T'}$, and $\overline{T'^2}$) at two different levels. In all cases, the interannual mean eddy fields are zonally modulated. Furthermore, the spatial distributions of eddy activity are generally similar in different Mars years, suggesting that meaningful climatological studies of this property of the Martian atmosphere can be conducted with the available amount of data.

In the northern hemisphere at $0.9 \cdot p_{\mathrm{ref}}$ during PRE and POST, we find that $\overline{v'T'}$ occurs in a roughly wave number 3 pattern to which the $\overline{T'^2}$ field bears some resemblance. At $0.5 \cdot p_{\mathrm{ref}}$, there may be a tendency to concentrate EKE above low-lying areas during all three eddying seasons and to put a $z'_{\mathrm{rms}N}$ maximum downstream of an EKE maximum in PRE and POST. The most notable feature of northern hemisphere PAUSE is the overall reduction in eddy strength relative to the other two seasons. The MY25 global dust storm, which significantly overlapped northern hemisphere PRE and PAUSE, evidently weakened activity in all eddy fields except $\overline{T'^2}$ but did not much change their spatial patterns (although it should be noted that *Montabone et al.* [2006] flagged the storm as one of the main areas of bias in their assimilation).

Spatial patterns of eddy activity tend to be similar across all three eddying seasons in the southern hemisphere, although eddy activity is clearly weaker during PAUSE than during the other seasons. The patterns are also similar between eddy fields at the same level, and despite differences in the details of their structures all four of them appear to have significant local maxima in the same two regions: roughly to the south of Tharsis and south or west of Hellas. This pattern is especially prominent for PRE and POST.

We also use teleconnection maps to define spatially localized eddy phase velocities, which allow us to document nonzonal propagation of eddies in MACDA. The eddy propagation tends to follow contours of topography, which is presumably why the propagation directions are largely independent of season. The topography-following behavior is also surface trapped. Although it seems easier to exhibit examples of such topography-following eddy propagation for the northern hemisphere than for the southern hemisphere, an apparent tendency for cyclonic eddy propagation at the surface within Hellas is particularly striking.

This study suggests three major areas of further inquiry, which are not necessarily independent. First, to what degree do the results presented here reflect the true behavior of the Martian atmosphere as opposed to the climatology and biases of the Mars GCM used to create MACDA? Data assimilation clearly changes the climatology of eddy activity relative to the unconstrained GCM, but how close does it bring the results to the truth? Further observing system simulation experiments may help address this issue.

Second, why do the eddy fields surveyed here have the properties that they do? An earlier GCM study [*Hollingsworth et al.*, 1996] indicates that the topography is important, with their diagnosis of the model output suggesting the effect of slopes on baroclinic instability as a possible mechanism. Although it is remarkable that linear baroclinic instability [*Blumsack and Gierasch*, 1972] may be able to tell us something about the spatial distribution of transient eddy activity on Mars, this relatively simple theory would benefit from elaboration with idealized GCM experiments to clarify the relationship between the zonal basic state, the stationary waves, and the climatology of transient eddy activity [e.g., *Chang*, 2006]. We plan to make such investigations a major direction of our future work.

Third, because of the role of particular baroclinic wave patterns in creating regional dust storms [*Hinson et al.*, 2012], progress on these questions may ultimately enhance simulations and understanding of the Martian dust cycle. As a complement to idealized studies of the dynamics of Martian baroclinic waves, it may be possible to increase observational understanding by building on Figure 1 with more thorough combined examinations of reanalysis data, imagery, and dust opacity retrievals. A particular focus of such work should be the role of tide-eddy interaction in the production of dust storms, first suggested by *Wang et al.* [2003]. Use of a Mars Climate Sounder-based reanalysis [e.g., *Navarro et al.*, 2014] and associated data sets would have the added advantage that dust opacity vertical structure information would be available for use in the study [*Kleinböhl et al.*, 2009].

Acknowledgments
The MACDA v1.0 data set, including information on the meridional and temporal distribution of TES retrievals assimilated to produce it, may be downloaded from the British Atmospheric Data Centre. We thank three colleagues for providing or discussing supporting information data sets used in this paper. Luca Montabone supplied a copy of the MACDA control simulation and a gridded topographic map at the same horizontal resolution as the MACDA data set, both of which are available upon request from the authors of *Montabone et al.* [2014]. Tim Titus provided his polar cap edge data set, which is available from him upon request (ttitus@usgs.gov). Bruce Cantor discussed the MOC image with us. The MOC image and TES dust opacity retrievals used in Figure 1 are available from the NASA Planetary Data System. We also thank two anonymous reviewers whose comments significantly improved the paper. Mooring was supported by the National Science Foundation Graduate Research Fellowship Program under grant DGE 1148900 and the National Oceanic and Atmospheric Administration, U.S. Department of Commerce under awards NA08OAR4320752 and NA14OAR4320106.

References

Banfield, D., B. J. Conrath, P. J. Gierasch, R. J. Wilson, and M. D. Smith (2004), Traveling waves in the Martian atmosphere from MGS TES nadir data, *Icarus*, *170*(2), 365–403, doi:10.1016/j.icarus.2004.03.015.

Barnes, J. R. (1980), Time spectral analysis of midlatitude disturbances in the Martian atmosphere, *J. Atmos. Sci.*, *37*(9), 2002–2015, doi:10.1175/1520-0469(1980)037<2002:TSAOMD>2.0.CO;2.

Barnes, J. R. (1981), Midlatitude disturbances in the Martian atmosphere: A second Mars year, *J. Atmos. Sci.*, *38*(2), 225–234, doi:10.1175/1520-0469(1981)038<0225:MDITMA>2.0.CO;2.

Barnes, J. R. (1984), Linear baroclinic instability in the Martian atmosphere, *J. Atmos. Sci.*, *41*(9), 1536–1550, doi:10.1175/1520-0469(1984)041<1536:LBIITM>2.0.CO;2.

Barnes, J. R., J. B. Pollack, R. M. Haberle, C. B. Leovy, R. W. Zurek, H. Lee, and J. Schaeffer (1993), Mars atmospheric dynamics as simulated by the NASA Ames general circulation model: 2. Transient baroclinic eddies, *J. Geophys. Res.*, *98*(E2), 3125–3148, doi:10.1029/92JE02935.

Barnes, J. R., M. S. Rucker, and D. Tyler, Jr. (2014), Transient eddies in the atmosphere of Mars: The crucial importance of water clouds, paper presented at Eighth International Conference on Mars, USRA, Pasadena, Calif. [Available at http://www.hou.usra.edu/meetings/8thmars2014/pdf/1447.pdf, 14–18 July.]

Basu, S., M. I. Richardson, and R. J. Wilson (2004), Simulation of the Martian dust cycle with the GFDL Mars GCM, *J. Geophys. Res.*, *109*, E11006, doi:10.1029/2004JE002243.

Basu, S., J. Wilson, M. Richardson, and A. Ingersoll (2006), Simulation of spontaneous and variable global dust storms with the GFDL Mars GCM, *J. Geophys. Res.*, *111*, E09004, doi:10.1029/2005JE002660.

Blumsack, S. L., and P. J. Gierasch (1972), Mars: The effects of topography on baroclinic instability, *J. Atmos. Sci.*, *29*(6), 1081–1089, doi:10.1175/1520-0469(1972)029<1081:MTEOTO>2.0.CO;2.

Cantor, B. A. (2007), MOC observations of the 2001 Mars planet-encircling dust storm, *Icarus*, *186*(1), 60–96, doi:10.1016/j.icarus.2006.08.019.

Cantor, B. A., P. B. James, M. Caplinger, and M. J. Wolff (2001), Martian dust storms: 1999 Mars Orbiter Camera observations, *J. Geophys. Res.*, *106*(E10), 23,653–23,687, doi:10.1029/2000JE001310.

Chang, E. K. M. (2006), An idealized nonlinear model of the Northern Hemisphere winter storm tracks, *J. Atmos. Sci.*, *63*, 1818–1839, doi:10.1175/JAS3726.1.

Chang, E. K. M., S. Lee, and K. L. Swanson (2002), Storm track dynamics, *J. Clim.*, *15*, 2163–2183, doi:10.1175/1520-0442(2002)015<02163:STD>2.0.CO;2.

Durran, D. R. (2010), *Numerical Methods for Fluid Dynamics: With Applications to Geophysics, Texts in Applied Mathematics*, vol. 32, Springer, New York.

Greybush, S. J., R. J. Wilson, R. N. Hoffman, M. J. Hoffman, T. Miyoshi, K. Ide, T. McConnochie, and E. Kalnay (2012), Ensemble Kalman filter data assimilation of Thermal Emission Spectrometer temperature retrievals into a Mars GCM, *J. Geophys. Res.*, *117*, E11008, doi:10.1029/2012JE004097.

Hinson, D. P., and H. Wang (2010), Further observations of regional dust storms and baroclinic eddies in the northern hemisphere of Mars, *Icarus*, *206*(1), 290–305, doi:10.1016/j.icarus.2009.08.019.

Hinson, D. P., H. Wang, and M. D. Smith (2012), A multi-year survey of dynamics near the surface in the northern hemisphere of Mars: Short-period baroclinic waves and dust storms, *Icarus*, *219*(1), 307–320, doi:10.1016/j.icarus.2012.03.001.

Hollingsworth, J. L., R. M. Haberle, J. R. Barnes, A. F. C. Bridger, J. B. Pollack, H. Lee, and J. Schaeffer (1996), Orographic control of storm zones on Mars, *Nature*, *380*(6573), 413–416, doi:10.1038/380413a0.

Hollingsworth, J. L., R. M. Haberle, and J. Schaeffer (1997), Seasonal variations of storm zones on Mars, *Adv. Space Res.*, *19*(8), 1237–1240, doi:10.1016/S0273-1177(97)00275-5.

Hoskins, B. J., and K. I. Hodges (2002), New perspectives on the Northern Hemisphere winter storm tracks, *J. Atmos. Sci.*, *59*(6), 1041–1061, doi:10.1175/1520-0469(2002)059<1041:NPOTNH>2.0.CO;2.

Hsu, H.-H. (1987), Propagation of low-level circulation features in the vicinity of mountain ranges, *Mon. Weather Rev.*, *115*(9), 1864–1892, doi:10.1175/1520-0493(1987)115<1864:POLLCF>2.0.CO;2.

Imamura, T., and H. Kobayashi (2009), Wavenumber spectra of planetary-scale disturbances in the Mars atmosphere, *Icarus*, *199*(2), 286–294, doi:10.1016/j.icarus.2008.09.021.

Kahre, M. A., J. L. Hollingsworth, and R. M. Haberle (2012), Simulating Mars' dust cycle with a Mars general circulation model: Effects of water ice cloud formation on dust lifting strength and seasonality, paper presented at Comparative Climatology of Terrestrial Planets, USRA, Boulder, Colo. [Available at http://www.lpi.usra.edu/meetings/climatology2012/pdf/8062.pdf, 25–28 June.]

Kavulich, M. J., Jr., I. Szunyogh, G. Gyarmati, and R. J. Wilson (2013), Local dynamics of baroclinic waves in the Martian atmosphere, *J. Atmos. Sci.*, *70*(11), 3415–3447, doi:10.1175/JAS-D-12-0262.1.

Kleinböhl, A., et al. (2009), Mars Climate Sounder limb profile retrieval of atmospheric temperature, pressure, and dust and water ice opacity, *J. Geophys. Res.*, *114*, E10006, doi:10.1029/2009JE003358.

Leovy, C., and Y. Mintz (1969), Numerical simulation of the atmospheric circulation and climate of Mars, *J. Atmos. Sci.*, *26*(6), 1167–1190, doi:10.1175/1520-0469(1969)026<1167:NSOTAC>2.0.CO;2.

Lewis, S. R., and P. L. Read (1995), An operational data assimilation scheme for the Martian atmosphere, *Adv. Space Res.*, *16*(6), 9–13, doi:10.1016/0273-1177(95)00244-9.

Lewis, S. R., P. L. Read, and M. Collins (1996), Martian atmospheric data assimilation with a simplified general circulation model: Orbiter and lander networks, *Planet. Space Sci.*, *44*(11), 1395–1409, doi:10.1016/S0032-0633(96)00058-X.

Lewis, S. R., M. Collins, and P. L. Read (1997), Data assimilation with a Martian atmospheric GCM: An example using thermal data, *Adv. Space Res.*, *19*(8), 1267–1270, doi:10.1016/S0273-1177(97)00280-9.

Lewis, S. R., P. L. Read, B. J. Conrath, J. C. Pearl, and M. D. Smith (2007a), Assimilation of thermal emission spectrometer atmospheric data during the Mars Global Surveyor aerobraking period, *Icarus*, *192*(2), 327–347, doi:10.1016/j.icarus.2007.08.009.

Lewis, S. R., L. Montabone, P. L. Read, P. Rogberg, R. J. Wilson, and M. D. Smith (2007b), Planetary waves in an assimilation of three Mars years of Thermal Emission Spectrometer data from Mars Global Surveyor, paper presented at Seventh International Conference on Mars, USRA, Pasadena, Calif. [Available at http://www.lpi.usra.edu/meetings/7thmars2007/pdf/3167.pdf, 9–13 July.]

Lewis, S. R., L. Montabone, P. L. Read, P. Rogberg, R. J. Wilson, and M. D. Smith (2008), Data assimilation of three Mars years of Thermal Emission Spectrometer observations: Large-scale transient and stationary waves, paper presented at Third International Workshop: Mars Atmosphere Modeling and Observations, USRA, Williamsburg, Va. [Available at http://oro.open.ac.uk/16936/1/Stephen_Lewis_2.pdf, 10–13 Nov.]

Lewis, S. R., D. P. Mulholland, P. L. Read, L. Montabone, R. J. Wilson, and M. D. Smith (2015), The solsticial pause on Mars: 1. A planetary wave reanalysis, *Icarus*, doi:10.1016/j.icarus.2015.08.039.

Martínez-Alvarado, O., L. Montabone, S. R. Lewis, I. M. Moroz, and P. L. Read (2009), Transient teleconnection event at the onset of a planet-encircling dust storm on Mars, *Ann. Geophys.*, *27*, 3663–3676, doi:10.5194/angeo-27-3663-2009.

Merlis, T. M., and T. Schneider (2009), Scales of linear baroclinic instability and macroturbulence in dry atmospheres, *J. Atmos. Sci.*, *66*(6), 1821–1833, doi:10.1175/2008JAS2884.1.

Mintz, Y. (1961), The general circulation of planetary atmospheres, in *The Atmospheres of Mars and Venus*, edited by W. W. Kellogg and C. Sagan, pp. 107–146, National Academy of Sciences-National Research Council, Washington, D. C. [Available at http://www.nap.edu/catalog/12424.html.]

Montabone, L., S. R. Lewis, P. L. Read, and D. P. Hinson (2006), Validation of Martian meteorological data assimilation for MGS/TES using radio occultation measurements, *Icarus*, *185*(1), 113–132, doi:10.1016/j.icarus.2006.07.012.

Montabone, L., K. Marsh, S. R. Lewis, P. L. Read, M. D. Smith, J. Holmes, A. Spiga, D. Lowe, and A. Pamment (2014), The Mars Analysis Correction Data Assimilation (MACDA) dataset v1.0, *Geosci. Data J.*, *1*(2), 129–139, doi:10.1002/gdj3.13.

Mulholland, D. P., S. R. Lewis, P. L. Read, J.-B. Madeleine, and F. Forget (2015), The solsticial pause on Mars: 2 Modelling and investigation of causes, *Icarus*, doi:10.1016/j.icarus.2015.08.038.

Navarro, T., F. Forget, E. Millour, and S. J. Greybush (2014), Detection of detached dust layers in the Martian atmosphere from their thermal signature using assimilation, *Geophys. Res. Lett.*, *41*, 6620–6626, doi:10.1002/2014GL061377.

Phillips, N. A. (1957), A coordinate system having some special advantages for numerical forecasting, *J. Meteorol.*, *14*, 184–185, doi:10.1175/1520-0469(1957)014<0184:ACSHSS>2.0.CO;2.

Pollack, J. B., R. M. Haberle, J. Schaeffer, and H. Lee (1990), Simulations of the general circulation of the Martian atmosphere: 1. Polar processes, *J. Geophys. Res.*, *95*(B2), 1447–1473, doi:10.1029/JB095iB02p01447.

Read, P. L., L. Montabone, D. P. Mulholland, S. R. Lewis, B. Cantor, and R. J. Wilson (2011), Midwinter suppression of baroclinic storm activity on Mars: observations and models, paper presented at Fourth International Workshop: Mars Atmosphere Modelling and Observations, Paris. [Available at http://oro.open.ac.uk/30843/1/read_paris2011.pdf, 8–11 Feb.]

Smith, M. D. (2004), Interannual variability in TES atmospheric observations of Mars during 1999–2003, *Icarus*, *167*(1), 148–165, doi:10.1016/j.icarus.2003.09.010.

Smith, M. D. (2008), Spacecraft observations of the Martian atmosphere, *Annu. Rev. Earth Planet. Sci.*, *36*, 191–219, doi:10.1146/annurev.earth.36.031207.124334.

Tanaka, H. L., and M. Arai (1999), Linear baroclinic instability in the Martian atmosphere: Primitive equation calculations, *Earth Planets Space*, *51*(3), 225–232, doi:10.1186/BF03352226.

Titus, T. N., and G. E. Cushing (2014), Monitoring the Mars polar caps during Mars years 24–28, paper presented at 45th Lunar and Planetary Science Conference, USRA, The Woodlands, Tex. [Available at http://www.hou.usra.edu/meetings/lpsc2014/pdf/2177.pdf, 17–21 March.]

Wallace, J. M., G.-H. Lim, and M. L. Blackmon (1988), Relationship between cyclone tracks, anticyclone tracks and baroclinic waveguides, *J. Atmos. Sci.*, *45*(3), 439–462, doi:10.1175/1520-0469(1988)045<0439:RBCTAT>2.0.CO;2.

Wang, H., and M. I. Richardson (2015), The origin, evolution, and trajectory of large dust storms on Mars during Mars years 24–30 (1999–2011), *Icarus*, *251*, 112–127, doi:10.1016/j.icarus.2013.10.033.

Wang, H., M. I. Richardson, R. J. Wilson, A. P. Ingersoll, A. D. Toigo, and R. W. Zurek (2003), Cyclones, tides, and the origin of a cross-equatorial dust storm on Mars, *Geophys. Res. Lett.*, *30*(9), 1488, doi:10.1029/2002GL016828.

Wang, H., R. W. Zurek, and M. I. Richardson (2005), Relationship between frontal dust storms and transient eddy activity in the northern hemisphere of Mars as observed by Mars Global Surveyor, *J. Geophys. Res.*, *110*, E07005, doi:10.1029/2005JE002423.

Wang, H., M. I. Richardson, A. D. Toigo, and C. E. Newman (2013), Zonal wavenumber three traveling waves in the northern hemisphere of Mars simulated with a general circulation model, *Icarus*, *223*(2), 654–676, doi:10.1016/j.icarus.2013.01.004.

Wilson, R. J. (2011), Dust cycle modeling with the GFDL Mars general circulation model, paper presented at Fourth International Workshop: Mars Atmosphere Modelling and Observations, Paris. [Available at http://www-mars.lmd.jussieu.fr/paris2011/abstracts/wilson_rj3_paris2011.pdf, 8–11 Feb.]

Wilson, R. J., D. Banfield, B. J. Conrath, and M. D. Smith (2002), Traveling waves in the northern hemisphere of Mars, *Geophys. Res. Lett.*, *29*(14), 29–1–29-4, doi:10.1029/2002GL014866.

Wilson, R. J., D. Hinson, and M. D. Smith (2006), GCM simulations of transient eddies and frontal systems in the Martian atmosphere, paper presented at Second International Workshop: Mars Atmosphere Modelling and Observations, Granada, Spain. [Available at http://www-mars.lmd.jussieu.fr/granada2006/abstracts/Wilson3_Granada2006.pdf, 27 Feb.–3 March.]

Wilson, R. J., S. R. Lewis, L. Montabone, and M. D. Smith (2008), Influence of water ice clouds on Martian tropical atmospheric temperatures, *Geophys. Res. Lett.*, *35*, L07202, doi:10.1029/2007GL032405.